ABSTRACT

Title of Thesis: EXPERIMENTAL STUDY OF LASER PRODUCED
                     ELECTRON BEAM

                     Yijie Huo, Master of Science, 2004

Thesis Directed By: Professor Patrick O'Shea
                     Department of Electrical and Computer Engineering

In this thesis, experimental studies are presented on longitudinal space-charge wave dynamics in space-charge dominated beams. Space-charge wave equations are derived using a cold-fluid model. Two kinds of perturbation are examined: an initial single peak pure-density perturbation and a small sinusoidal density modulation. The theoretical evolution of these two kinds of perturbation is compared with WARP RZ simulations. A new experimental method using a laser to produce such an initial pure-density perturbation is studied. The propagation of the resulting space-charge waves in University of Maryland Electron Ring (UMER) is measured and analyzed for different combinations of main beam current and perturbation current. Good agreement is achieved in all the theoretical analyses, simulation results and experimental measurements. In addition to the longitudinal space-charge wave dynamics study, the reconstruction of the transverse phase space of the photoemission beam is also reported.

EXPERIMENTAL STUDY OF LASER PRODUCED ELECTRON BEAM

By

Yijie Huo

Thesis submitted to the Faculty of the Graduate School of the
University of Maryland, College Park, in partial fulfillment
of the requirements for the degree of
Master of Science
2004

Advisory Committee:
        Professor Patrick G. O'Shea, Chair/Advisor
        Professor Victor L. Granatstein
        Dr. Rami A. Kishek

Dedication

To my parents.

Acknowledgements

I would like to acknowledge many people who have contributed to this project and helped me during the two years' study and research.

The first person I want to thank is my advisor, Professor Patrick O'Shea. I want to thank him not only because of his broad knowledge and his profound insights, but also because of his decent, warm, sensitive and caring personality. He gave me a promising and significant research project, and strong encouragement and full support. I would like to thank him for his trust and confidence in me and his appreciation of my work. I also want to thank Professor M. Reiser who is the senior authority in our field. I always benefit from his constructive criticism on my work.

I wish to thank Dr. R.A. Kishek who gave me a lot of help on my research work. He has spent an enormous amount of time with me to solve the simulation problems and work on the theory. I wish to thank Dr. I Haber who gave me a lot of help in the simulations. I wish to thank Dr. Y. Zou who gave me a lot of help in the theoretical analysis. I wish to thank Dr. D. Feldman who gave me a lot of help in the laser setup and photocathode theory. I wish to thank Dr. H. Li who taught me how to use UMER in detail and gave me a lot of help in my experiments.

I wish to thank Dr. S. Bernal, Dr. M. Walker and B. Quinn who are the excellent experimental, mechanical and electrical experts. I wish to thank Dr. Y. Cui, J. Neumann, J. Harris, G. Bai, K. Tian, Dr. Y. Miao, T. Firestone and N. Moody for their kind assistance and useful discussions.

I wish to thank Professor V. Granatstein for serving on my thesis exam committee.

Finally, I give my greatest thanks to my parents for their unconditional support and love.

Table of Contents

List of Tables

List of Figures

Chapter 1: Introduction

1.1 Background

Charged particle beams have a diverse history of applications [1, 2]. Physics of low intensity beams have been well studied since the 1920's [3], while applications for high intensity beams have dramatically increased in recent years. Several applications require beams with unprecedented intensity and quality, e.g. linacs for heavy ion fusion (HIF) [4, 5, 6], spallation neutron source [7] and free electron lasers (FEL) [8].

The study of beam physics in space-charge dominated regime is of special interest to many scientists, since "all beams of interest are born in space-charge dominated regime" [9]. As the beam is accelerated, the emittance plays an increasingly dominant role in the beam dynamics. However, non-linear space-charge induced phase space distortions (transverse and longitudinal) will persist as the beam is accelerated and result in irreversible emittance growth and diminished intensity. The appearance of various space-charge waves introduces a complex array of modes, resonances, instabilities and radiations that can potentially degrade beam qualities and limit applications. Many of these effects are not well understood. In this thesis, a new method to generate controlled initial density perturbation by laser is discussed. The evolution of the longitudinal perturbation is experimentally studied and compared with theoretical analyses and simulations.

Modern accelerators such as heavy ion fusion driver are very large and expensive. However, to study beam physics, one can build a less expensive and smaller electron ring

to simulate the behavior of the heavy ion beam systems. The low energy electron beam can have almost the same β (velocity of particles/velocity of light), generalized perveance K (defined below) and intensity parameter χ (defined below) as the high energy heavy ion beams. Some experimental values of the parameters for heavy ion beams and electron beams are listed in Table 1.1. Therefore, from a theoretical point of view, both beams have similar physical properties. The University of Maryland Electron Ring (UMER) is designed under this concept to study transverse and longitudinal dynamics of space-charge dominated beams. The schematic layout of UMER is shown in Figure 1.1.

Table 1.1 Parameter comparison between HIF beam and UMER electron beam

Beam parameters	Heavy ion beam	Electron beam
Energy	10 GeV	10 keV
$\beta = v / c$	0.3	0.2
Current	5 kA	100 mA
Mass	$3.7*10^5$ m_e	m_e
Charge state	+1	-1
Generalized perveance K	$8.7*10^{-4}$	$1.5*10^{-3}$
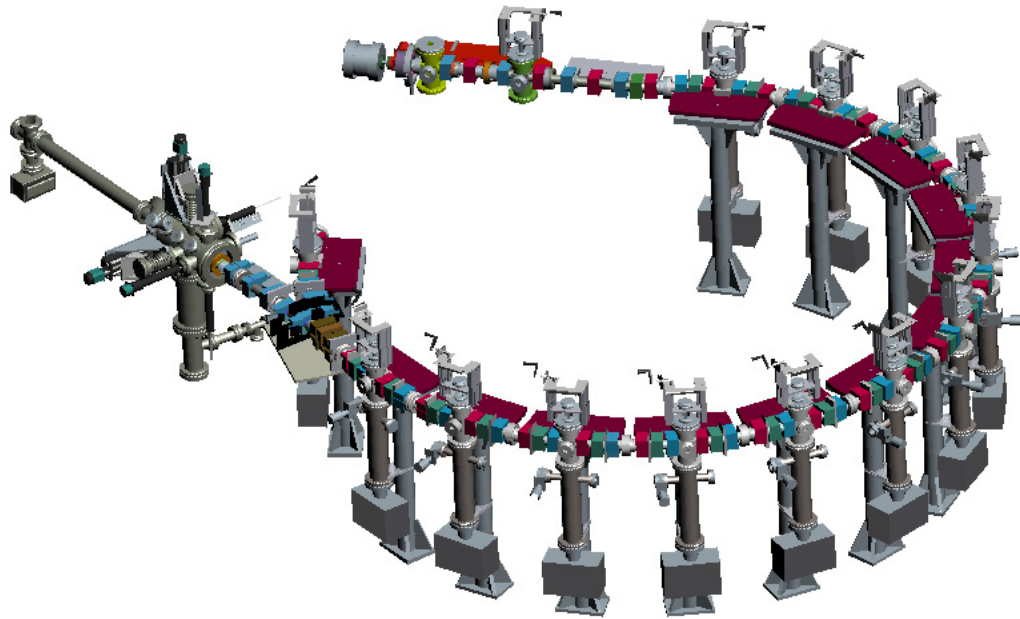
Figure 1.1 Current UMER layout: 2/3 ring + injector + temporary extractor

The Kapchinsky-Vladimirsky (K-V) transverse beam envelope equation in a symmetric focusing channel can be described as [2, 10]

$$\frac{d^2R}{dz^2} + \kappa_0(z)R - \frac{K}{R} - \frac{\varepsilon^2}{R^3} = 0,$$ (1.1)

where R is the beam radius, z is the traveling distance, κ_0 is the external focusing strength, ε is the unnormalized effective (4*RMS) emittance, and K is the generalized perveance. The intensity parameter χ is defined as the ratio of the internal space-charge force to the external focusing force, i.e.

$$\chi = \frac{K}{k_0^2 R^2},$$ (1.2)

where k_0 is the zero-current betatron oscillation wave number. The range of χ is from 0 to 1. If χ is less than 0.5, the beam is emittance-dominated in the transverse direction. If χ is larger than 0.5, the beam is space-charge-dominated in the transverse direction. The UMER can operate in a very wide regime, from space-charge-dominated region to emittance-dominated region, corresponding to the intensity parameter χ ranging from 0.99 to 0.2. The betatron tune depression and plasma tune enhancement vs. the intensity parameter are plotted in Figure 1.2.
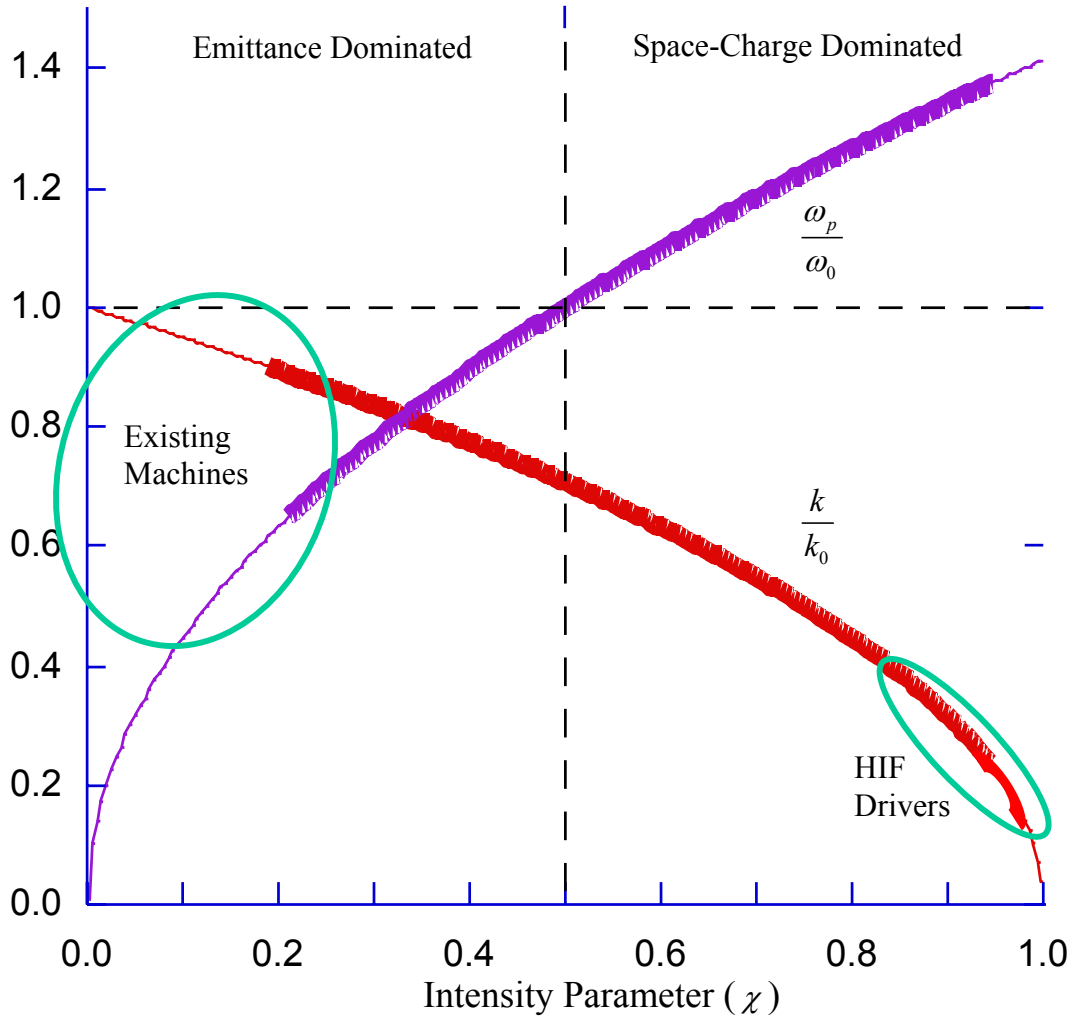
Figure 1.2 The betatron tune depression (k/k_0) and plasma tune enhancement (ω_p/ω_0) with increasing intensity parameter. The intensity parameter χ for UMER is ranging from 0.2 to 0.99. The beam with $\chi > 0.5$ is in the space-charge dominated regime. The beam with $\chi < 0.5$ is in the emittance dominated regime.

Similarly, the longitudinal envelope equation for a parabolic line charge density profile beam is given by [2, 11, 12]

$$z_m'' + \kappa_{z0} z_m - \frac{K_L}{z_m^2} - \frac{\varepsilon_{zz'}^2}{z_m^3} = 0,$$ (1.3)

where $2 \cdot z_m$ is the bunch length, $\kappa_{z0} z_m$ is the longitudinal focusing term and $\varepsilon_{zz'}$ represents the unnormalized effective longitudinal emittance, $\varepsilon_{zz'} = 5\tilde{\varepsilon}_{zz'}$, $\tilde{\varepsilon}_{zz'}$ is the unnormalized RMS longitudinal emittance, and K_L is the longitudinal generalized perveance defined as

$$K_L = \frac{3}{2} \frac{g N r_c}{\beta_0^2 \gamma_0^5}.$$ (1.4)

Here g is the geometry parameter, N is the number of particles in the bunch, and $r_c = q^2 / 4\pi\varepsilon_0 mc^2$ is the classical particle radius. Similarly, the longitudinal intensity parameter χ_L can be define as

$$\chi_L = \frac{K_L}{\kappa_{z0} z_m^3},$$ (1.5)

which ranges from 0 to 1. If χ_L is less than 0.5, the beam is emittance dominated in the longitudinal direction. If χ_L is larger than 0.5, the beam is space-charge dominated in the longitudinal direction. In UMER, the longitudinal generalized perveance is from $1.2*10^{-2}$ m ($I = 100\ mA,\ R = 1cm$) to $2.6*10^{-4}$ m ($I = 0.6\ mA,\ R = 0.08\ cm$), which corresponds to the beam energy at 10 keV, pipe radius of 2.54 cm, and pulse width of 100 ns. If we assume that the energy spread of the electron beam is 10 eV, the RMS unnormalized longitudinal emittance $\tilde{\varepsilon}_{zz'}^2 = \langle z^2 \rangle \langle z'^2 \rangle$ is about $1.6*10^{-3}$ m. The longitudinal intensity parameter χ_L, therefore, is from 0.998 to 0.92 for UMER electron beams. This

calculation shows that the electron beam in UMER is extremely space-charge dominated in the longitudinal direction. Some detailed information about the longitudinally space-charge dominated beams can be found in John Harris' master thesis [11].

1.2 Motivation

The transport of intense beams with high beam quality is very important in advanced accelerator researches. Space-charge effects in this kind of beam play a crucial role in the beam dynamics, particularly in the formation of longitudinal space-charge waves. *The purpose of this thesis is to understand longitudinal space-charge wave physics of space-charge dominated beams*.

Although a lot of researches have been done on the longitudinal space-charge wave dynamics since 1980's, the generation of perturbations always contains both line charge density modulation and energy modulation. In 1993, J.G. Wang and D.X. Wang performed a series of experiments using the Maryland Electron Beam Transport facility [13, 14]. Space-charge waves were produced at the gridded cathode of the electron gun by creating local perturbations of beam velocity and current. The measurement of wave velocity agrees well with the theory. At the beam edge, some interesting phenomena such as the transmission and reflection of space-charge wave were observed.

In the late 1990's, H. Suk and Y. Zou began to study the space-charge wave dynamics in a resistive-wall pipe [15]. As before, a grid-voltage perturbation generates a localized perturbation to produce space-charge waves. The perturbation currents were measured by current monitors, and the propagation of the space-charge wave was studied experimentally in linear region. Y. Zou measured the growth rate/decay rate of the

longitudinal energy width of the space-charge waves with the new designed retarding voltage energy analyzer in both linear and nonlinear regime [16]. In the linear regime, the energy width of the slow wave was observed growing, while the energy width of the fast wave decaying. In the nonlinear regime, the decay rate of the energy width associated with the fast wave was more complicated. Furthermore, the experiment with a conductive pipe showed that the growth rate of energy width is zero, as expected.

Similar investigations have also been conducted in other labs. Some of the most important work was done by D.A. Callahan in 1997 in Lawrence Livermore National Laboratory [17]. An RZ particle-in-cell code was setup to simulate the longitudinal wall impedance instability in a heavy-ion fusion driver. The growth rate of instability was calculated in both theory and simulation. The results showed that the longitudinal wall impedance instability is not a serious threat to the success of heavy-ion driven inertial confinement fusion.

In all these previous experimental studies, the perturbations were produced by perturbing the cathode grid voltage. The combination of energy modulation and charge density modulation makes it hard to obtain the exact initial condition needed for theoretical calculations, and difficult to understand the physics concepts clearly. Therefore, the generation of an initial longitudinal pure-density perturbation is import in the study of space-charge wave dynamics.

In this thesis, a new experimental method to generate initial pure-density modulation is discussed. An ultraviolet laser impinges on the photocathode. The photoemission electrons, whose energy distribution is almost the same as that of the thermionic emission electrons, form the initial longitudinal pure-density perturbation.

The photoemission schematic and the perturbed beam current are shown in Figures 1.3 and 1.4, respectively. The initial pure-density perturbation gives a clear initial boundary condition, and allows direct comparisons with the theory, simulation and experiment. The new WARP RZ simulation of the longitudinal space-charge waves in UMER agrees with the theory and experiment.

Further research can be carried out using the knowledge obtained here, such as the longitudinal resistive-wall instability, the noise response of space-charge dominated beams, and the radiative properties of longitudinal modulated beams.
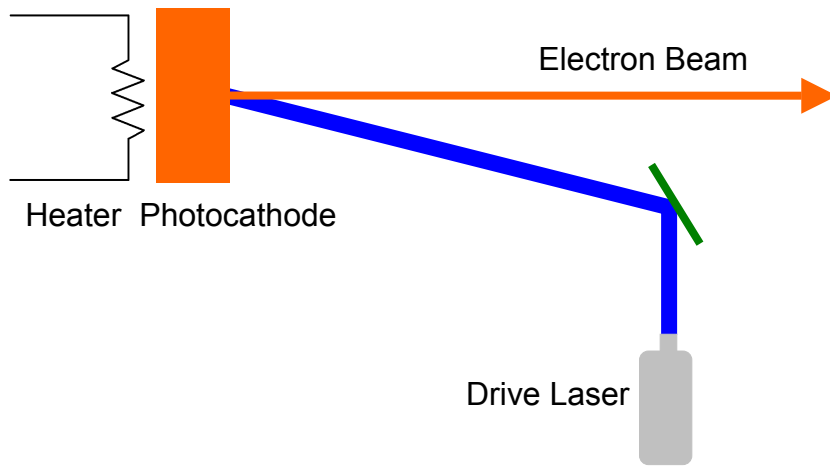
Figure 1.3 Schematic for photoemission

Figure 1.4 Beam current of the photo and thermionic emission electron beam measured by Bergoz current transformer

1.3 Organization of the thesis

In Chapter 2, the theoretical analysis of space-charge wave dynamics is studied first; then the WARP 2D (RZ) simulation results are discussed. The single density perturbation and small sinusoid modulation of the beam current are examined according to the analytical and simulation results. The experiments of the longitudinal space-charge wave are presented in Chapter 3. The sound speeds are calculated for the different combinations of main beam currents and perturbation currents, and compared with the theory and simulation. In Chapter 4, the reconstruction of the transverse phase space of an 8 mA photoemission electron beam is discussed. Finally, a conclusion is given in Chapter 5.

Chapter 2: Theory and Simulation of Longitudinal Space-Charge Wave

The theoretical analysis and simulation results of the longitudinal space-charge wave produced by pure-density perturbation are presented first.

In the first part, the single particle dynamics is studied and the dispersion equation is given. The two eigenvalues of the fast space-charge wave and slow space-charge wave are shown and the sound speed equation is derived by using the cold-fluid model. The analytical results of the evolution of the localized perturbation are calculated and plotted under the initial pure-density modulation assumption.

In the second part, the WARP 2D (RZ) simulation results are shown. The single density perturbation and small sinusoidal modulation beam are simulated and plotted. The simulation results are compared with the theoretical predictions.

2.1 Theory of longitudinal space-charge wave

2.1.1 Single particle dynamics in a sinusoidal density modulation beam

From plasma theory, for a small sinusoidal modulation of the electron beam, the single particle dynamics equation is expressed by a harmonic oscillation equation as

$$\ddot{s} + \omega_p^2 s = 0, \tag{2.1}$$

where s(t) denotes the particle displacement from the equilibrium position in the moving

beam frame as a function of time t, and the plasma frequency $\omega_p = \left(\dfrac{q^2 n_0}{\varepsilon_0 m \gamma_0^3} \right)^{1/2}$ [18]. The

solution of this harmonic oscillation equation is

$$s(t) = C_1 e^{i\omega_p t} + C_2 e^{-i\omega_p t},$$
(2.2a)

$$\dot{s}(t) = i\omega_p C_1 e^{i\omega_p t} - i\omega_p C_2 e^{-i\omega_p t},$$
(2.2b)

where c_1 and c_2 are complex coefficients determined by the initial condition. For a pure-

density modulation at the initial time, t_0, the boundary condition can be written as

$$s(t_0) = L_1 \cos(\omega t_0),$$
(2.3a)

$$\dot{s}(t_0) = 0.$$
(2.3b)

So the coefficients can be expressed by

$$c_1 = \frac{L_1}{2} e^{i(\omega - \omega_p)t_0},$$
(2.4a)

$$c_2 = \frac{L_1}{2} e^{i(\omega + \omega_p)t_0}.$$
(2.4b)

By substituting the coefficients into equation (2.2a), the displacement of a single particle

can be derived as

$$s(t) = \frac{L_1}{2} \left[e^{i(\omega - \omega_p)t_0} e^{i\omega_p t} + e^{i(\omega + \omega_p)t_0} e^{-i\omega_p t} \right].$$
(2.5)

Since the relationship between the beginning time t_0 and distance z is given by

$$t_0 = t - \frac{z}{v_0},$$
(2.6)

where v_0 is the main beam velocity , equation (2.5) can be expressed by t and z in the

form

$$s(t,z) = \frac{L_1}{2} e^{i\omega t} \left[e^{-i\frac{(\omega-\omega_p)}{v_0}z} + e^{-i\frac{(\omega+\omega_p)}{v_0}z} \right] = \frac{L_1}{2} e^{i\omega t} \left[e^{-ik_f z} + e^{-ik_s z} \right], \qquad (2.7)$$

where the two wave numbers k_f and k_s are given by

$$k_f = \frac{\omega - \omega_p}{v_0}, \qquad (2.8a)$$

$$k_s = \frac{\omega + \omega_p}{v_0}. \qquad (2.8b)$$

They also satisfy the dispersion relation, which applies for such modulation in a cold beam and which is given by

$$(\omega - kv_0)^2 = \omega_p^2. \qquad (2.9)$$

The group velocity v_g in the laboratory frame can be derived from the dispersion relation as

$$v_g = \frac{\partial \omega}{\partial k} = v_0, \qquad (2.10)$$

which means the whole wave energy propagates at v_0. The phase velocity can be derived from equation (2.8a) and (2.8b), as

$$v_f = \frac{\omega}{k_f} = \frac{v_0}{1 - (\omega_p / \omega)}, \qquad (2.11a)$$

$$v_s = \frac{\omega}{k_s} = \frac{v_0}{1 + (\omega_p / \omega)}. \qquad (2.11b)$$

Transforming the phase velocity into the beam frame, one obtains

$$v_+ = v_f - v_0 = v_0 \frac{\omega_p}{\omega - \omega_p}, \qquad (2.12a)$$

$$\text{v}_- = \text{v}_s - \text{v}_0 = -\text{v}_0 \frac{\omega_p}{\omega + \omega_p}. \tag{2.12b}$$

The equations (2.12a) and (2.12b) show that there are two kinds of waves, one being a fast space-charge wave, since the phase velocity is greater than the beam velocity ($v_f > v_0$ or $v_+ > 0$); the other being a slow space-charge wave, since the phase velocity is less than the beam velocity ($v_s < v_0$ or $v_- < 0$). The displacements of particles is correlated with the velocity v(t,z), the line space-charge density Λ(t,z) and the current I(t,z). The superposition of the fast and slow waves leads to modulation of the electron beam current.

2.1.2 Derivation of sound speed using a one dimensional cold-fluid model

In the previous section, the single particle dynamics equation is derived under an ideal condition. In this section, a more realistic description is considered by assuming an infinitely long matched cylindrical electron beam with beam radius a inside a conducting drift tube of radius b [2]. We assume a perturbation in the form of $e^{i(\omega t - kz)}$. The total line-charge density Λ, velocity v and beam current I are defined as

$$\Lambda(z,t) = \Lambda_0 + \Lambda_1 e^{i(\omega t - kz)}, \tag{2.13a}$$

$$\text{v}(z,t) = \text{v}_0 + \text{v}_1 e^{i(\omega t - kz)}, \tag{2.13b}$$

$$I(z,t) = I_0 + I_1 e^{i(\omega t - kz)}, \tag{2.13c}$$

where the relationship of these three quantities is

$$I = \Lambda \text{v}. \tag{2.14}$$

Note that the subscripts 0 and 1 represent the unperturbed and perturbed quantities respectively. By neglecting the second-order terms, one obtains from (2.13a), (2.13b), (2.13c) and (2.14)

$$I_0 = \Lambda_0 v_0, \tag{2.15a}$$

$$I_1 = \Lambda_0 v_1 + \Lambda_1 v_0. \tag{2.15b}$$

The one-dimensional cold-fluid model, which neglects the longitudinal momentum spread of the beam, is used. The continuity equation yields

$$\frac{\partial (\Lambda v)}{\partial z} + \frac{\partial \Lambda}{\partial t} = 0. \tag{2.16}$$

Substitution of equation (2.13a), (2.13b) and (2.15b) into equation (2.16) yields

$$\Lambda_1 = \frac{kI_1}{\omega}. \tag{2.17}$$

The relativistic form of the longitudinal motion equation can be written as

$$\gamma_0^3 m \frac{dv}{dt} = qE_z,$$

or

$$\frac{\partial v}{\partial z} v_0 + \frac{\partial v}{\partial t} = \frac{q}{\gamma_0^3 m} E_z, \tag{2.18}$$

where E_z is the longitudinal electric field produced by the space-charge waves in this ideal case and is expressed as $E_z = E_s \exp\left[i(\omega t - kz)\right]$. Substitution of equation (2.13b) into equation (2.18) yields

$$v_1 = -i \frac{qE_s}{\gamma_0^3 m (\omega - kv_0)}. \tag{2.19}$$

Using equations (2.17) and (2.19), one obtains from (2.15b)

$$E_s = i\frac{\gamma_0^3 m}{q\Lambda_0}\frac{(\omega - kv_0)^2}{\omega}I_1. \tag{2.20}$$

The longitudinal electric field E_s can be also derived from Maxwell's equations as

$$E_s = -\frac{g}{4\pi\varepsilon_0}\left(\frac{\partial\Lambda}{\partial z} + \frac{1}{c^2}\frac{\partial I}{\partial t}\right), \tag{2.21}$$

where the geometry factor g is defined as

$$g = 2\ln\frac{b}{a}, \tag{2.22}$$

for the space-charge dominated beam, where $\Lambda/C \gg \varepsilon/k_0$. Substitution of equation (2.13a), (2.13c) and (2.17) into equation (2.21) yields

$$E_s = i\frac{g}{4\pi\varepsilon_0}\left(\frac{k^2}{\omega} - \frac{\omega}{c^2}\right)I_1. \tag{2.23}$$

Equaling equation (2.20) and equation (2.23), the dispersion relation can be derived as

$$\frac{\gamma_0^3 m}{q\Lambda_0}\frac{(\omega - kv_0)^2}{\omega} = \frac{g}{4\pi\varepsilon_0}\left(\frac{k^2}{\omega} - \frac{\omega}{c^2}\right),$$

or

$$(\omega - kv_0)^2 - \gamma_0^2 C_s^2 k^2\left(1 - \frac{\omega^2}{k^2 c^2}\right) = 0, \tag{2.24}$$

where the wave speed C_s is defined as

$$C_s = \left(\frac{qg\Lambda_0}{4\pi\varepsilon_0\gamma_0^5 m}\right)^{1/2}. \tag{2.25}$$

The speed of the wave, C_s, is called the 'sound speed', in analogy to the mathematically equivalent problem of the propagation of a perturbation in a non-relativistic cold fluid.

Since in the UMER system, the difference between the phase velocities of the two space-charge waves is very small compared to the beam velocity v_0, we can assume that $\omega \approx kv_0$. The equation (2.24) can be written in a simple way as

$$\left(\omega - kv_0\right)^2 - C_s^2 k^2 = 0. \tag{2.26}$$

The solution of this equation is

$$\omega = k\left(v_0 \pm C_s\right). \tag{2.27}$$

The phase velocities of two space-charge waves are

$$v_f = \frac{\omega}{k_+} = v_0 + C_s,$$

$$v_s = \frac{\omega}{k_+} = v_0 - C_s. \tag{2.28}$$

As an example, we substitute parameters for UMER in equation (2.25). It is assumed that the beam current is 20 mA and the electron energy is 10 keV. The mean beam radius is about 0.4 cm and the pipe radius is 2.54 cm. The sound speed can be calculated from theory as, $C_s = 1.26*10^6$ m/s.

2.1.3 The evolution of space-charge waves produced by initial density perturbation

The sound speed of the space-charge wave is calculated in the previous section. The evolution of the density perturbation, velocity perturbation and current perturbation is discussed in this section.

The one-dimensional cold-fluid model is still used to solve the localized space-charge wave in the time domain. Unlike solving for the eigenmodes from the dispersion equations of a sinusoidal wave in the previous section, specific solutions are calculated

under the given initial and boundary conditions [16, 19]. The total line-charge density Λ, velocity v and beam current I are defined as

$$\Lambda(z,t) = \Lambda_0(z,t) + \Lambda_1(z,t), \tag{2.29a}$$

$$v(z,t) = v_0(z,t) + v_1(z,t), \tag{2.29b}$$

$$I(z,t) = I_0(z,t) + I_1(z,t), \tag{2.29c}$$

where the subscripts 0 and 1 represent the unperturbed and perturbed quantities respectively. Considering the initial and boundary conditions, the localized velocity and current perturbation are determined by

$$v_1(0,t) = \delta v_0 h(t), \tag{2.30a}$$

$$I_1(0,t) = \eta I_0 h(t), \tag{2.30b}$$

where h(t) is any smooth function with amplitude of unity, which represents the shape of the perturbation; δ and η are small, positive quantities to specify the strength of the perturbation. With the relationship of these three quantities in equation (2.14) and omitting the second order term, the density perturbation is determined by

$$\Lambda_1(0,t) = (\eta - \delta)\Lambda_0 h(t) \tag{2.31}$$

Substituting equation (2.29a), (2.29b), (2.30a) and (2.31) into the continuity equation and the momentum transfer equation (2.16) and (2.18) and omitting the second-order term, one obtains

$$\frac{\partial \Lambda_1}{\partial t} + v_0 \frac{\partial \Lambda_1}{\partial z} + \Lambda_0 \frac{\partial v_1}{\partial z} = 0, \tag{2.32a}$$

$$\frac{\partial v_1}{\partial t} + v_0 \frac{\partial v_1}{\partial z} \approx \frac{e}{m\gamma^3} E_z = -\frac{eg}{4\pi\varepsilon_0 m\gamma^5} \frac{\partial \Lambda_1}{\partial z}, \tag{2.32b}$$

19

where $e/(m\gamma^3)$ denotes the ratio of the charge and the longitudinal mass of the charged particles with γ being the relativistic factor, $E_z(z,t)$ is the longitudinal electrical field induced by the AC component of the beam current, which is $\dfrac{-g}{4\pi\varepsilon_0\gamma^2}\dfrac{\partial\Lambda_1}{\partial z}$ in the long wavelength limit, i.e., the perturbation wavelength is much larger than the pipe radius, ε_0 is the permittivity of free space, and g is the geometry factor.

By applying the double Laplace transform from time-space domain to the k-s domain, the differential equations (2.32a) and (2.32b) can be converted to an algebraic equation of $\tilde{v}_1, \tilde{\Lambda}_1$. Applying the initial condition, the perturbed beam parameters are determined by

$$
\begin{aligned}
\tilde{\Lambda}_1(k,s) &= \left[\tilde{h}(s)/D\right]\left[s\eta i_0 + k(\eta-\delta)\Lambda_0\left(v_0^2-C_s^2\right)\right], \\
\tilde{v}_1(k,s) &= \left[\tilde{h}(s)/D\right]\left\{s\left[\delta v_0^2+(\eta-\delta)C_s^2\right]+k\delta v_0\left(v_0^2-C_s^2\right)\right\},
\end{aligned}
\tag{2.33}
$$

where C_s is the velocity of space-charge wave in the beam frame, defined in equation (2.25), and $D=(s+kv_0)^2-(kC_s)^2$ is the dispersion function. The $I=\Lambda v$ is transformed to

$$
\tilde{I}_1(k,s) = v_0\tilde{\Lambda}_1(k,s)+\Lambda_0\tilde{v}_1(k,s).
\tag{2.34}
$$

Using the inverse Laplace transform, the result is transferred from k-s domain to time-space domain. The perturbed beam density, velocity and current in the real time-space domain are given by

$$
\begin{aligned}
\Lambda_1(z,t) = &-\frac{\Lambda_0}{2}\left[\delta\frac{v_0}{C_s}-(\eta-\delta)\right]h\left(t-\frac{z}{v_0-C_s}\right) \\
&+\frac{\Lambda_0}{2}\left[\delta\frac{v_0}{C_s}+(\eta-\delta)\right]h\left(t-\frac{z}{v_0+C_s}\right),
\end{aligned}
\tag{2.35a}
$$

$$v_1(z,t) = +\frac{v_0}{2}\left[\delta - (\eta - \delta)\frac{C_s}{v_0}\right]h\left(t - \frac{z}{v_0 - C_s}\right)$$
$$+\frac{v_0}{2}\left[\delta + (\eta - \delta)\frac{C_s}{v_0}\right]h\left(t - \frac{z}{v_0 + C_s}\right), \tag{2.35b}$$

$$I_1(z,t) = -\frac{i_0}{2}\left[\delta\frac{v_0}{C_s} - \eta + (\eta - \delta)\frac{C_s}{v_0}\right]h\left(t - \frac{z}{v_0 - C_s}\right)$$
$$+\frac{i_0}{2}\left[\delta\frac{v_0}{C_s} + \eta + (\eta - \delta)\frac{C_s}{v_0}\right]h\left(t - \frac{z}{v_0 + C_s}\right). \tag{2.35c}$$

These equations show that each perturbed beam parameter consists of two terms: One is the fast wave with h(t-z/(v$_0$+c$_s$)), the other one is the slow wave with h(t-z/(v$_0$-c$_s$)). The amplitude and polarity of each wave are determined by the coefficients.

Considering the pure-density perturbation case, the velocity perturbation is zero, $\delta = 0$. Therefore, equation (2.35a), (2.35b) and (2.35c) can be expressed as

$$\Lambda_1(z,t) = \frac{\Lambda_0}{2}\eta\left[h\left(t - \frac{z}{v_0 - C_s}\right) + h\left(t - \frac{z}{v_0 + C_s}\right)\right], \tag{2.36a}$$

$$v_1(z,t) = \frac{C_s}{2}\eta\left[-h\left(t - \frac{z}{v_0 - C_s}\right) + h\left(t - \frac{z}{v_0 + C_s}\right)\right], \tag{2.36b}$$

$$i_1(z,t) = \frac{i_0}{2}\eta\left[\left(1 - \frac{C_s}{v_0}\right)h\left(t - \frac{z}{v_0 - C_s}\right) + \left(1 + \frac{C_s}{v_0}\right)h\left(t - \frac{z}{v_0 + C_s}\right)\right]. \tag{2.36c}$$

In non-relativistic case, the kinetic energy of the electron beam, W, can be calculated as

$$W = \frac{1}{2}mv^2 = \frac{1}{2}m(v_0 + v_1)^2. \tag{2.37}$$

By neglecting the second-order term, the energy perturbation can be expressed as

$$W_1 = W - W_0 \approx mv_0 v_1(z,t). \tag{2.38}$$

With the velocity expression in equation (2.36), the energy perturbation is written as

$$W_1(z,t) = \frac{1}{2} m v_0 C_s \eta \left[-h\left(t - \frac{z}{v_0 - C_s} \right) + h\left(t - \frac{z}{v_0 + C_s} \right) \right]. \tag{2.39}$$

The perturbation profiles of electron energy, velocity, line charge density and current in equation (2.39), (2.36b), (2.36a) and (2.36c), are respectively plotted in Figure 2.1 [20]. Several assumptions are made in this calculation. The main beam current is 20 mA and assumed to be infinitely long. The perturbation current is a Gaussian pulse and the magnitude of the perturbation is 2 mA. The beam energy is 10 keV. The beam radius is 0.5 cm and the pipe radius is 2.54 cm. A uniform magnetic field is applied to transversely confine the matched beam. At the beginning, the energy distribution of the pure-density modulated beam as well as the velocity distribution is uniform. The line charge density curve has the same shape as the current curve. After the beam propagates several meters, the initial Gaussian density perturbation spreads and splits into two peaks, which is due to the propagation of the fast and slow space-charge waves. The original uniform energy and velocity curves exhibit a positive pulse, which represents the fast space-charge wave, and a negative pulse which represents the slow space-charge wave in this case. In the Current vs. Time figures, the magnitude of the first perturbation is larger than that of the second one. This is because the figure is plotted in the laboratory frame. The difference between the velocities of the fast and slow space-charge waves generates the different beam currents for the same density perturbations. If the current is plotted in the beam frame, the currents will be equal, which will be shown in the simulation results in the later section of this chapter. At 20 m from the beginning, the single Gaussian current perturbation splits into two small Gaussian perturbations. As calculated in the previous section , the sound speed is $1.26 * 10^6$ m/s.
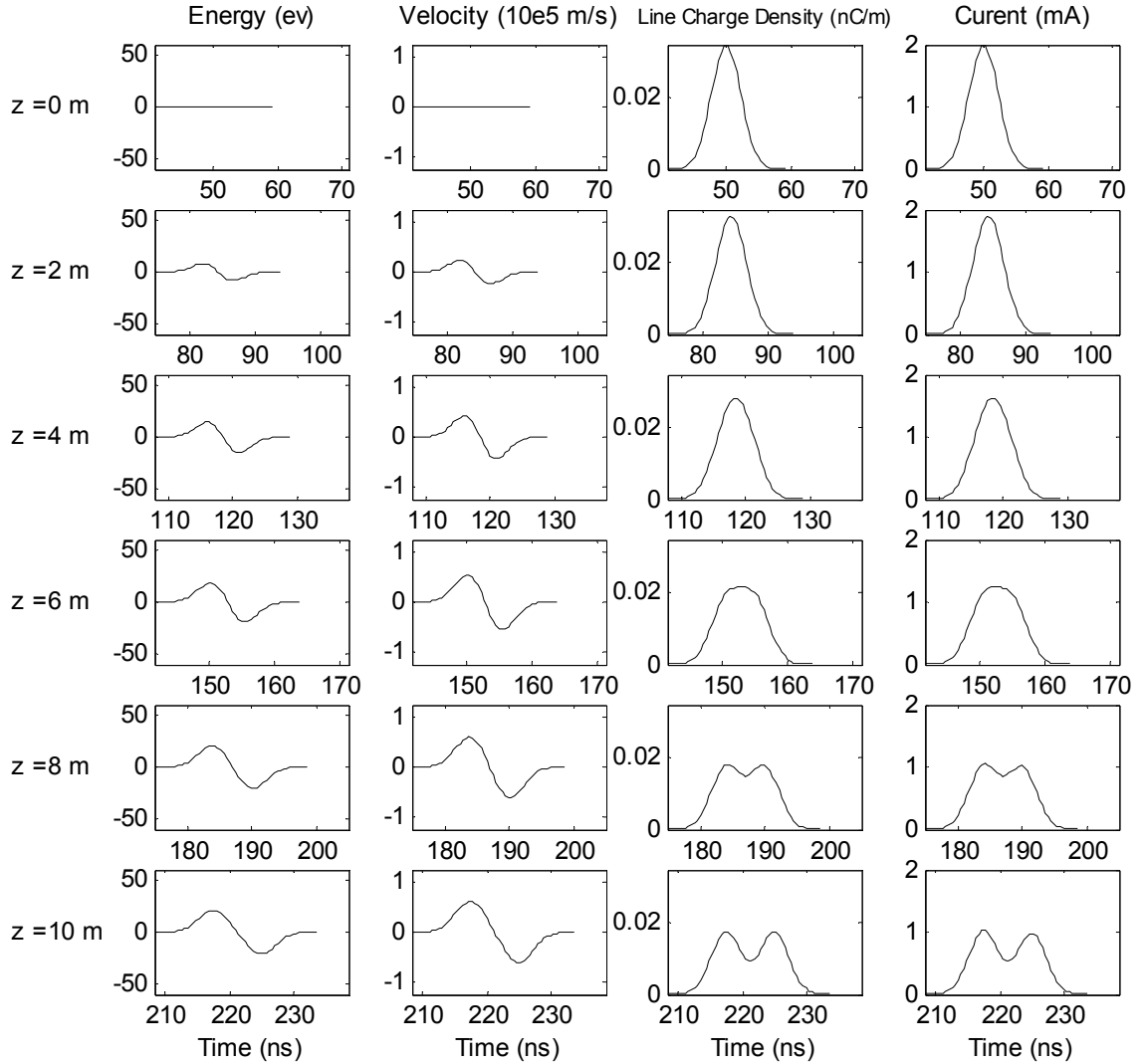
Figure 2.1 Evolution of space-charge waves produced by initial Gaussian pure-density perturbation. The figures are taken at location from 0 m to 22 m with adjacent spacing of 2 m. The figures in each column correspond to electron energy, electron velocity, line charge density and current of the perturbation. All the figures are plotted in the rest laboratory frame. (Continued on next page)
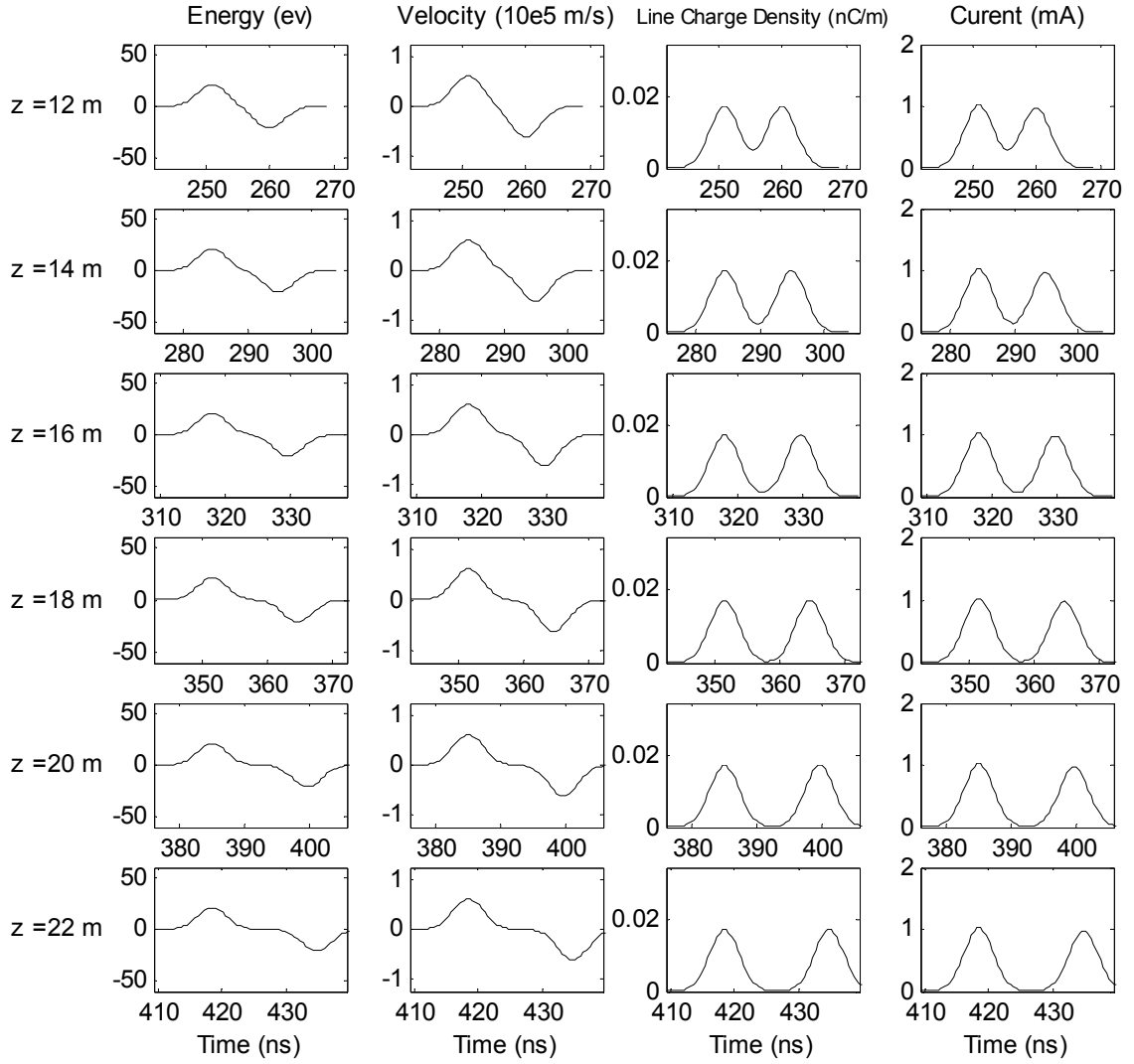
Figure 2.1 (Continued) Evolution of space-charge waves produced by initial Gaussian pure-density perturbation.

Using equations (2.36) and (2.39), the evolution of the small sinusoidal perturbation can be plotted and shown in Figure 2.2. The magnitude of the sinusoidal modulation current is 2 mA. Other parameters are same as before. At the beginning, the energy distribution is uniform for the pure-density modulation electron beam. After 7-meter-propagation, the original density modulation changes into the energy modulation [21]. The perturbed line charge density and current curve almost go to zero and the perturbation energy and velocity curve reach a maximum. Then after another 7-meter-propagation, the perturbed energy distribution goes back to zero and the perturbed current goes reaches a maximum as before.

In order to show the detailed information of the transformation from all the density modulation to the energy modulation, a set of figures are plotted around 6.75 m and shown in Figure 2.3. The density modulation of the perturbed beam goes to zero. However, the current curve never goes to zero. This is also because the velocities of the fast and slow space-charge wave are not same. This result also can be seen from equation (2.36), where the coefficients of the current modulation are not same.
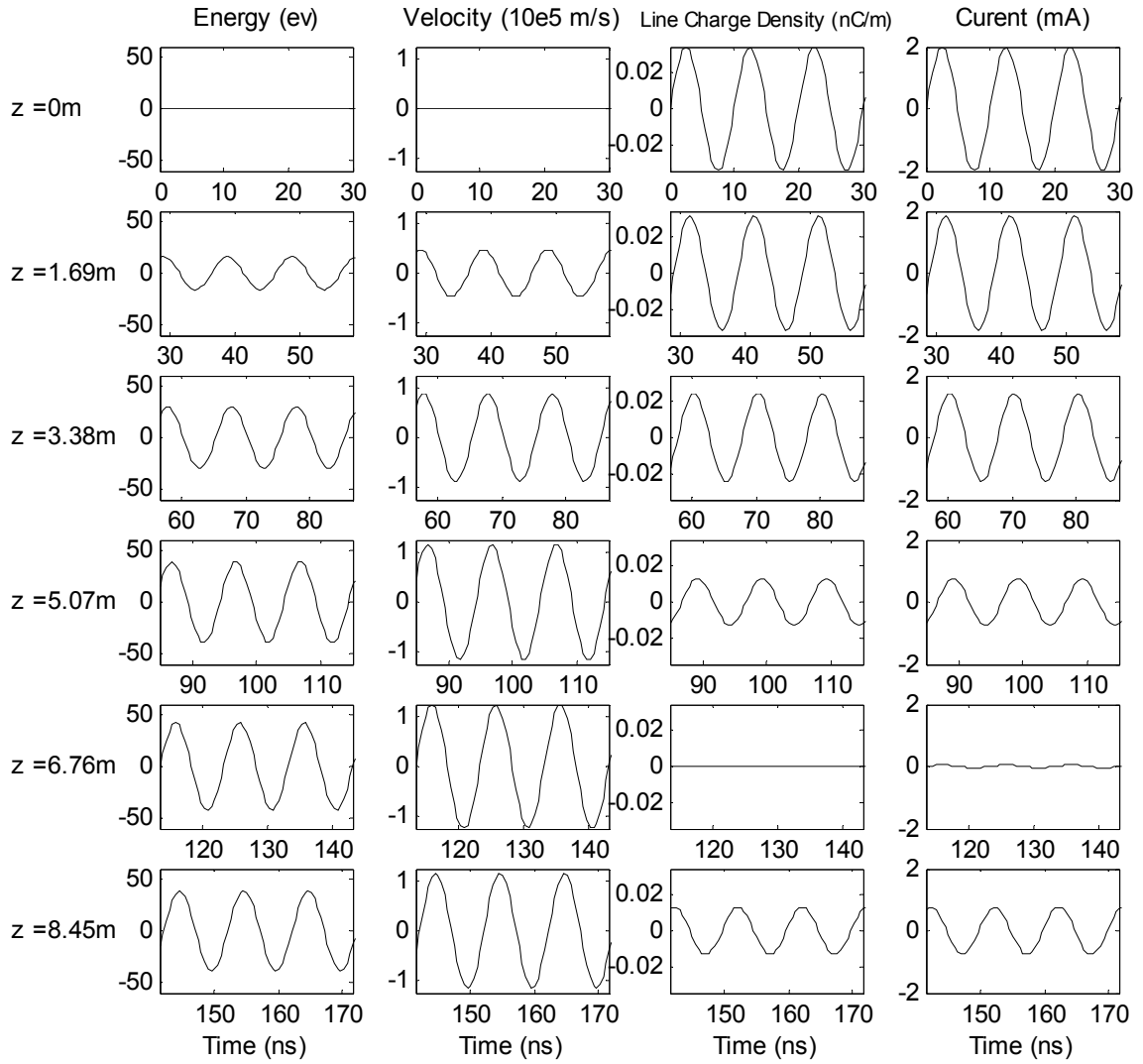
Figure 2.2 Evolution of a sinusoidal perturbation. The figures are taken at location from 0 m to 18.6 m with adjacent spacing of 1.69 m. The figures in each column correspond to electron energy, electron velocity, line charge density and current of the perturbation. All the figures are plotted in the rest laboratory frame. (Continued on next page)

26

Figure 2.2 (Continued) Evolution of a sinusoidal perturbation.

27

Figure 2.3 The transformation of a pure-density sinusoidal modulation to energy modulation. The figures are taken at location from 6.65 m to 6.85 m with adjacent spacing 0.05 m. The figures in each column correspond to the electron energy and velocity, the line charge density and the current of the perturbation. All the figures are plotted in the rest laboratory frame.

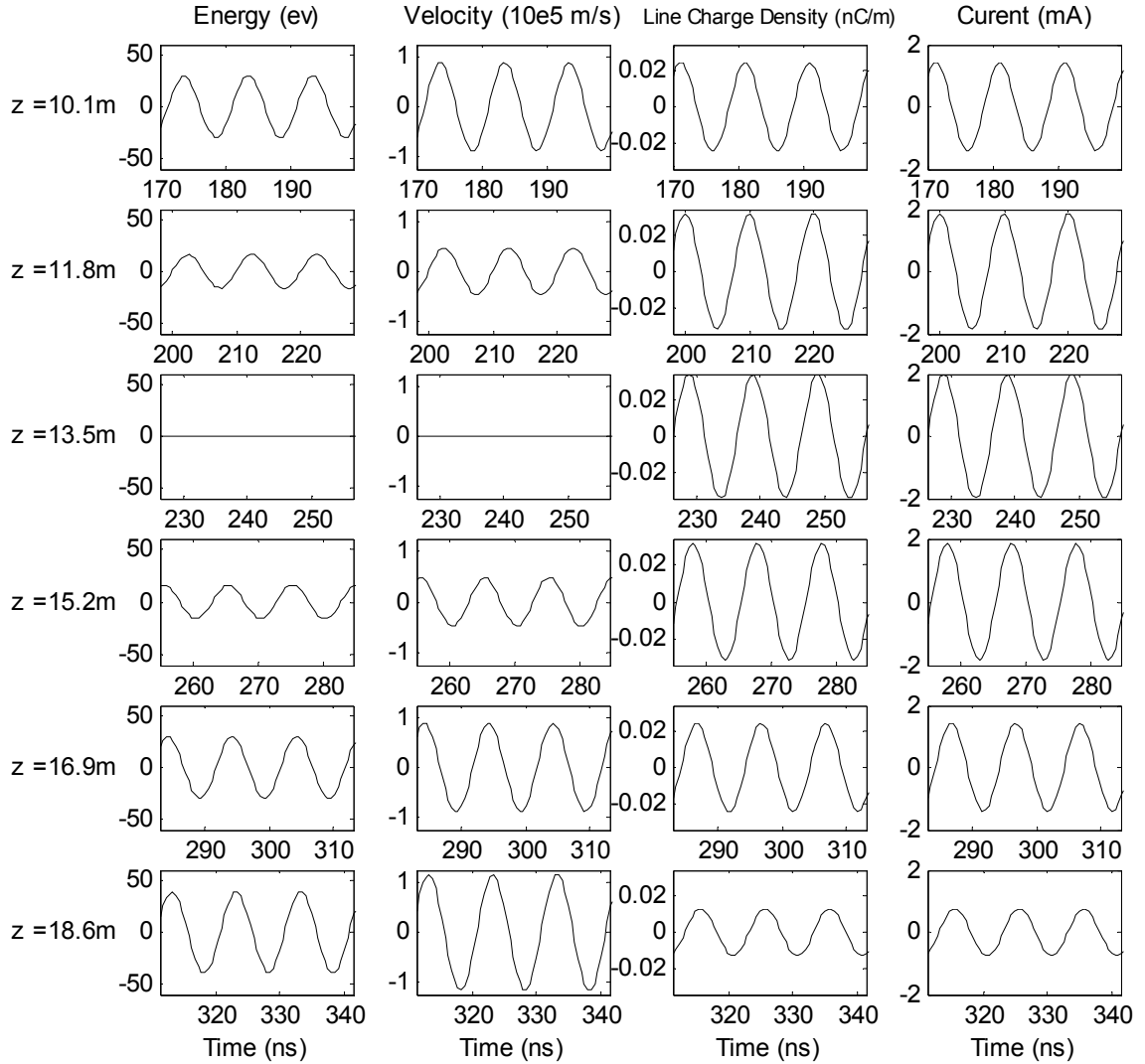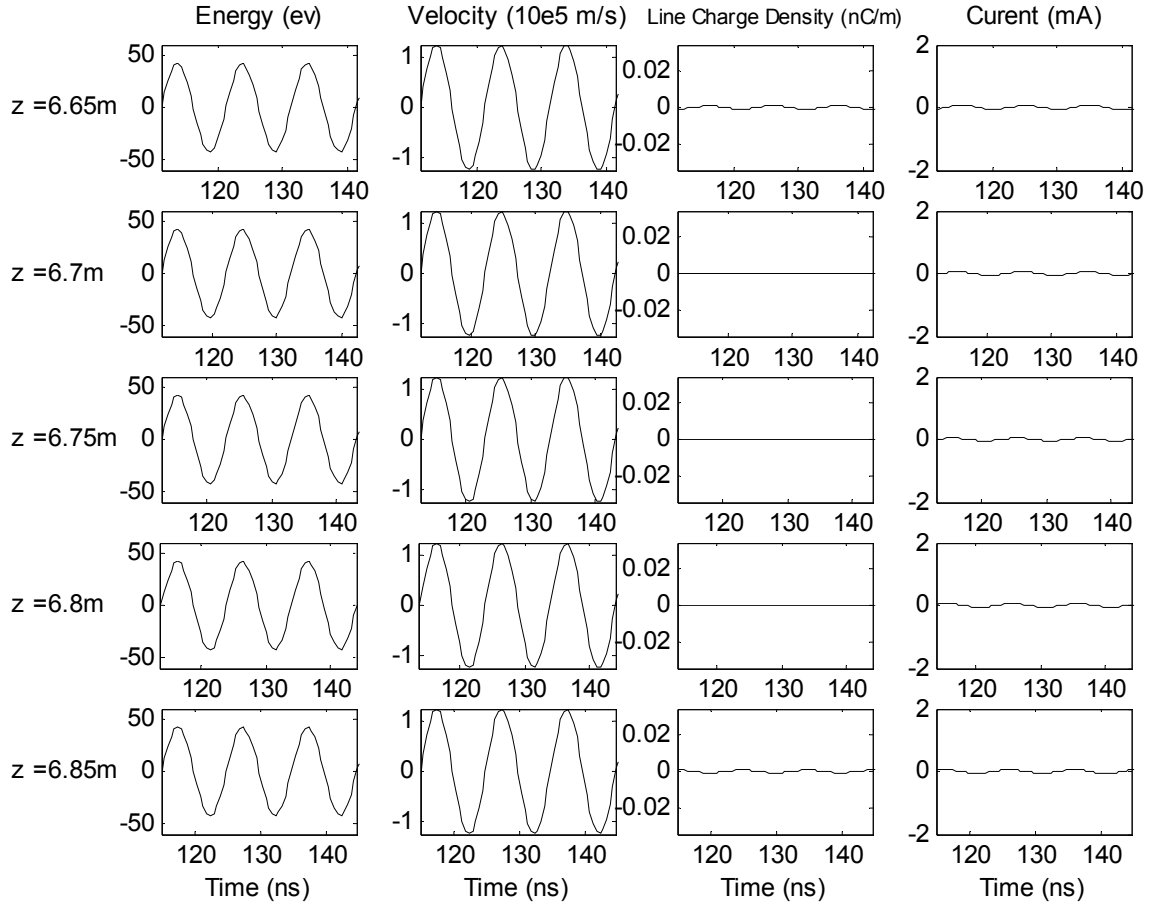## 2.2 Simulation of longitudinal space-charge wave

To test the analytic theory studied in the previous section, we conduct numerical simulations of the longitudinal space-charge waves using the WARP code. WARP is a particle in cell (PIC) code, which uses thousands of macro-particles to do the numerical calculation. Each macro-particle represents a large number of real particles in the experiment. The initial density and velocity distribution of micro-particles are given. The potential and electric field is calculated from the distribution of macro-particles and boundary conditions. The macro-particles are pushed by the electric field to new positions with a new velocity distribution. Then the calculations of new electric field and new particle distribution are iterated until the end of simulation.

A WARP 2-D (RZ) simulation program is used [22]. The simulations assume that the main beam is a rectangular 20 mA beam with pulse width of 100 ns; the pipe radius is 2.54 cm; the electron energy is 10 keV. The magnitude of the uniform magnetic field is calculated to matching the 20 mA electron beam. 500,000 particles are used in the simulation. The longitudinal direction is divided into 256 grids and the radius direction is separated to 64 grids.

2.2.1 Simulation of electron beam propagation with initial single density perturbation

The first simulation case is a 20 mA 5 ns parabolic density perturbation at the center of the main beam. The current curve is shown in the first plot in Figure 2.4. Although the nonlinear effects are very significant, the basic physical concept is shown

very clearly in this case. The simulation results are shown in Figure 2.4. At the end of the simulation, the single parabolic perturbation splits into two perturbations. The positive and negative peaks in the energy vs. position figures also represent the fast and slow space-charge waves respectively.

z = 0 m

z = 2 m

z = 4 m

z = 6 m

z = 8 m

z = 10 m

z = 12 m

z = 14 m

Figure 2.4 The simulation results of the large perturbed beam evolution. The figures in the first and third column are the current of the perturbation beam in the beam frame. The figures in the second and fourth column are the electron velocity of the perturbation beam in the rest laboratory frame. Each pair of current and velocity figures is taken at same location, z = 0, 2, 4, 6, 8, 10, 12, and 14 meters.

In Figure 2.4, at z = 8 m, the current curve has three peaks. This is due to the initial perturbation distribution. In this simulation case, a parabolic perturbation is assumed. In the analytical calculation in the previous section, since the Gaussian perturbation is assumed at the beginning, none of this kind of three-peak phenomenon appears. As discussed in the next chapter, there is no this kind of three peaks phenomena in the experimental results. So the initial pure-density perturbation in the experiment is more like a Gaussian perturbation.

The current curves in the analytical calculation are asymmetrical. However, the current curves in each figure are symmetrical in the numerical simulation. As discussed in the previous section, the velocity of the fast and slow space-charge wave is different in the rest laboratory frame. So the current is asymmetrical in the analytical calculation, which is calculated in the laboratory frame. In the numerical analysis, the current curve is plot in the beam frame, where velocities of fast and slow wave are symmetrical. So the current curve is also symmetrical.

Since the perturbation current is the same as the main beam current, the nonlinear effect is also significant in this case. One phenomena is that extra spikes appear at the tail of the fast wave and the head of the slow wave, which can be seen at z = 14 m. This phenomenon may also be induced from the instability of the numerical calculation. In order to eliminate this kind of effect, a small perturbation current is simulated and shown in Figure 2.5. The magnitude of the perturbation current is only 2 mA. The sound speed can be calculated from the simulation result, $Cs=1.3*10^6$ m/s, which agrees with the theory calculation.

z = 0 m

z = 2 m

z = 4 m

z = 6 m

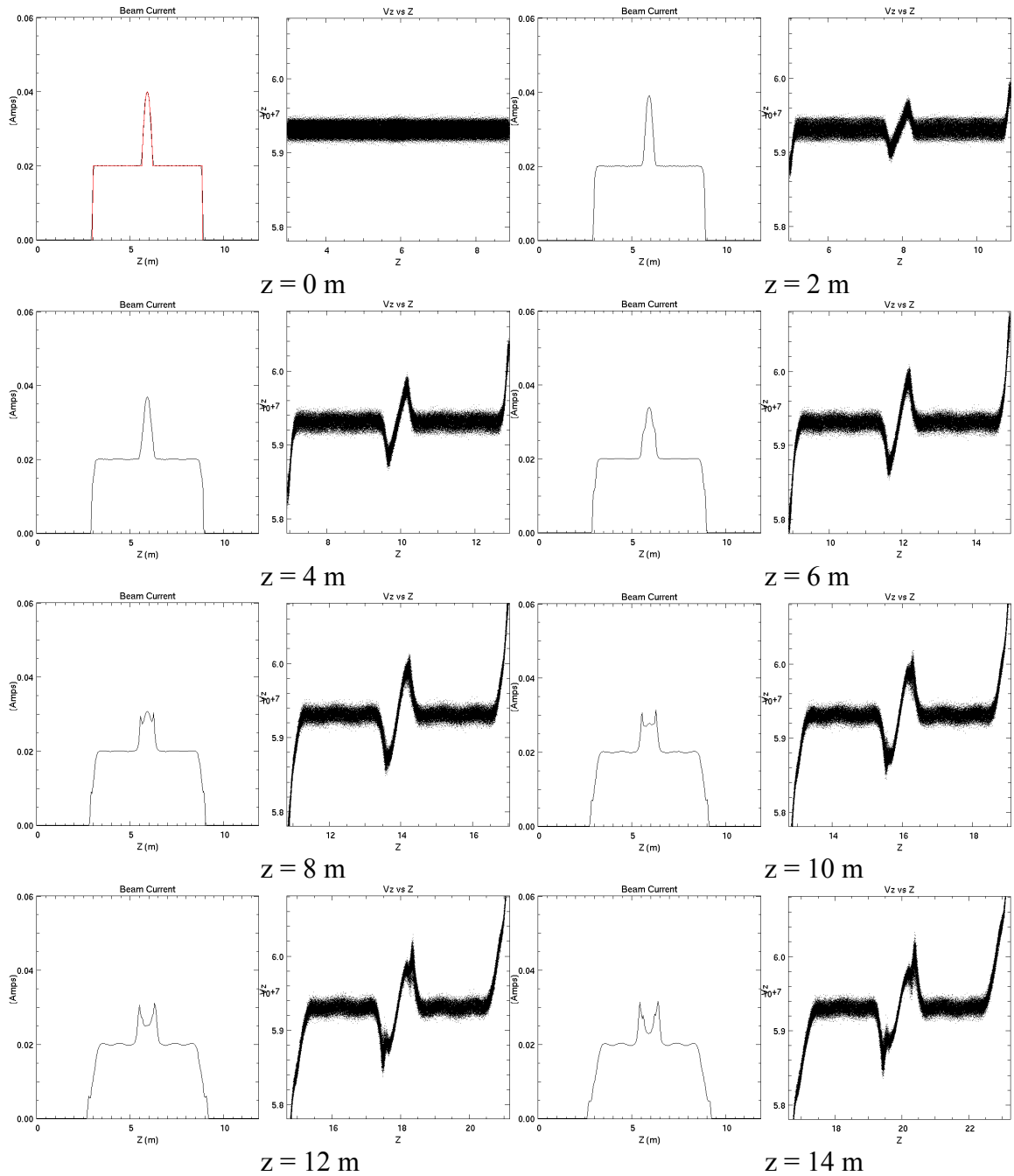z = 8 m

z = 10 m

z = 12 m

z = 14 m

Figure 2.5 The simulation results of the small perturbed beam evolution. The figures in the first and third column are the current of the perturbation beam in the beam frame. The figures in the second and fourth column are the electron velocity of the perturbation beam in the rest laboratory frame. Each pair of current and velocity figures is taken at same location, z = 0, 2, 4, 6, 8, 10, 12, and 14 meter.

2.2.2 Simulation of electron beam propagation with a small sinusoidal modulation

Another simulation is the 20 mA main beam with small sinusoidal modulation. The beam current is shown in the first plot of Figure 2.6, where the peak-to-peak magnitude of the perturbation is 4 mA. In these figures, the modulation of current (line charge density) transfers to the modulation of velocity (energy) and then goes back.

At z = 7 m the density modulation disappears and the velocity (energy) modulation goes to its maximum, which is shown in Figure 2.7. At z = 14 m the density modulation goes back to its maximum and the velocity (energy) modulation disappears. This phenomena is same as the theoretical prediction, in which the density modulation transfers to energy modulation at z = 6.8 m. From the simulation results, the transfer distance is also 6.8 meter.

z = 0 m   z = 2 m

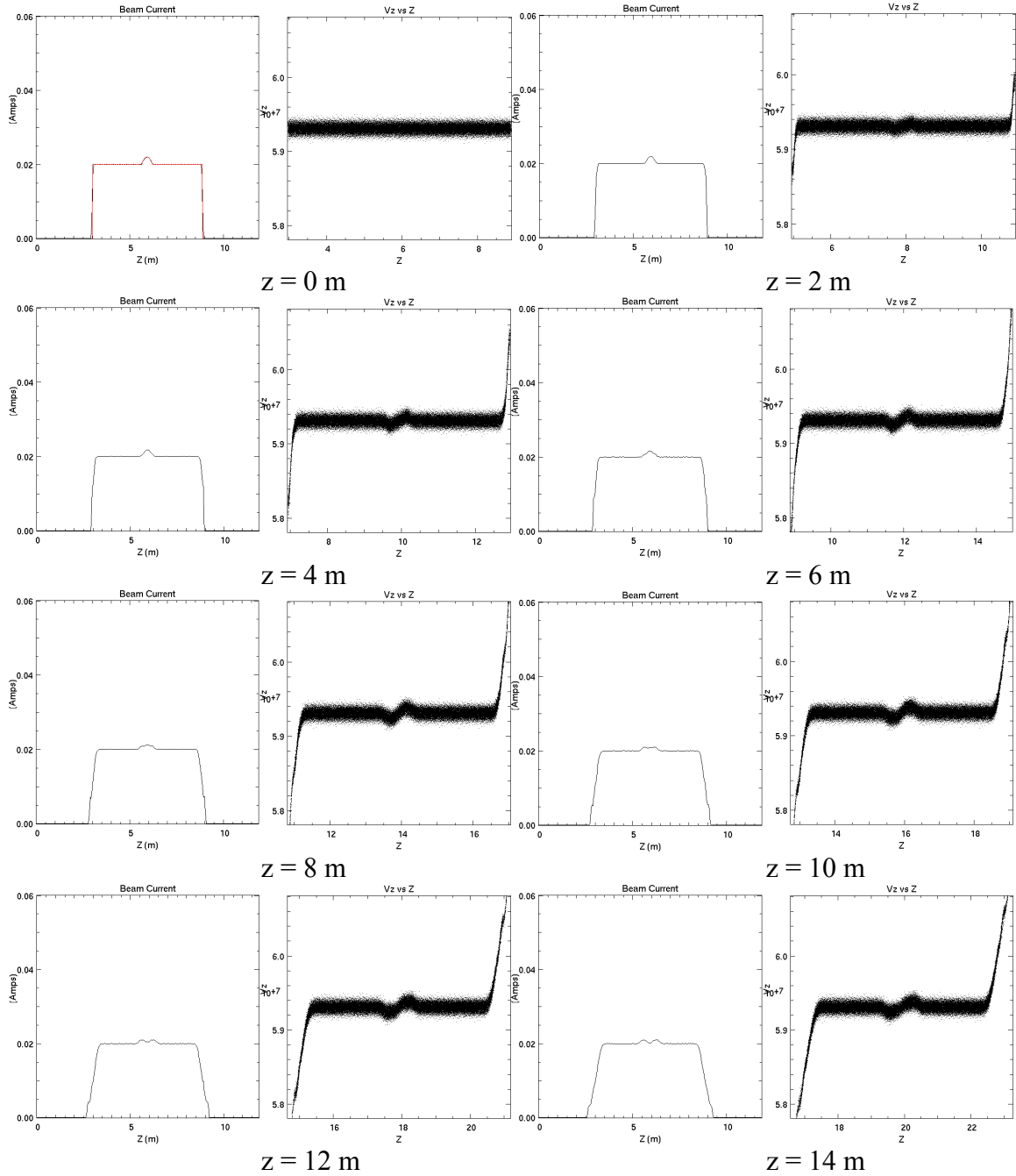z = 4 m   z = 6 m

z = 8 m   z = 10 m

z = 12 m   z = 14 m
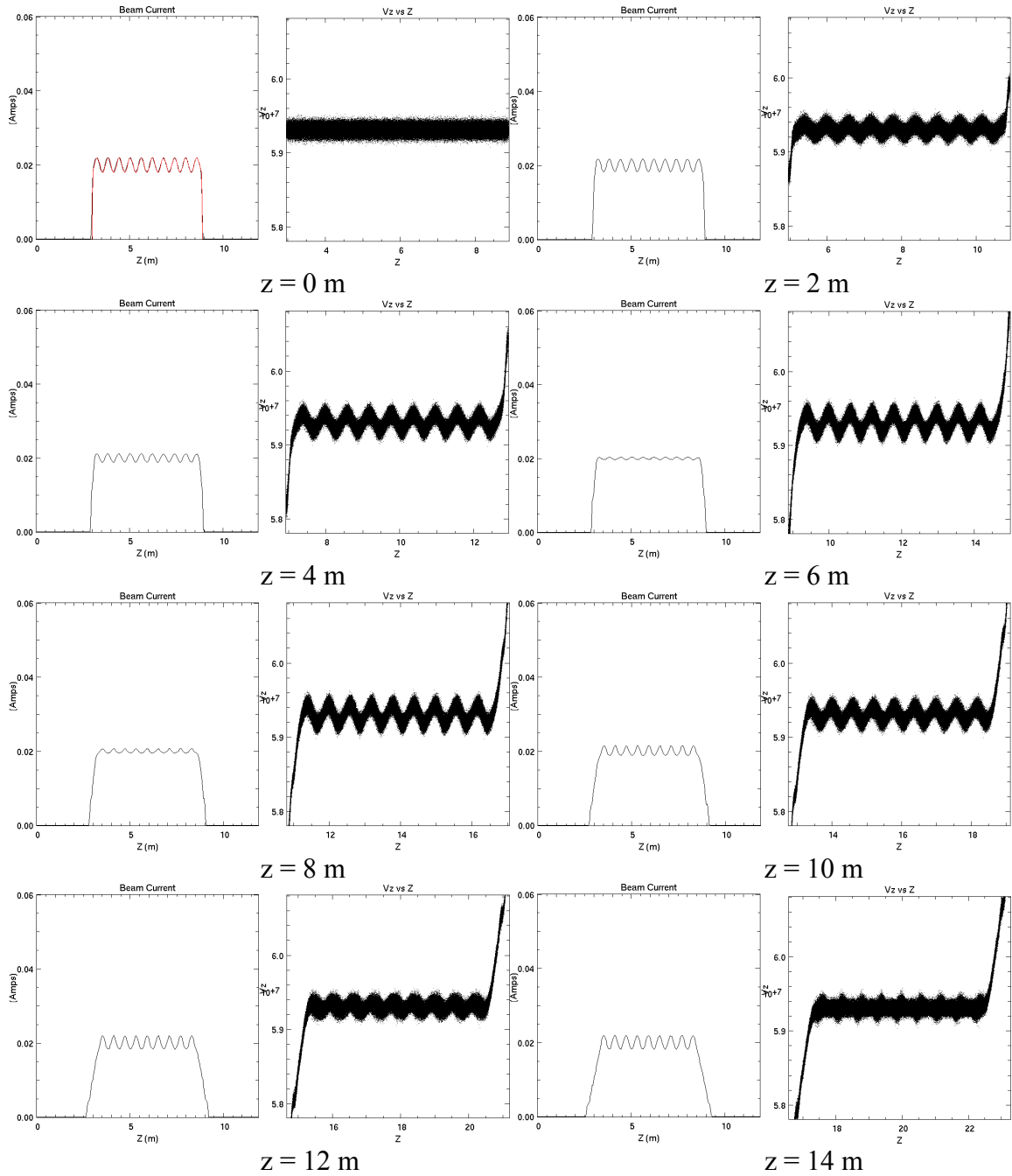
Figure 2.6 Simulation results of the small sinusoidal modulation beam evolution. The figures in the first and third column are the current of the perturbed beam in the beam frame. The figures in the second and fourth column are the electron velocity of the perturbed beam in the rest laboratory frame. Each pair of current and velocity figures is taken at same location, z = 0, 2, 4, 6, 8, 10, 12, and 14 meter.

z = 0 m

z = 7 m

z = 14 m

z = 20 m
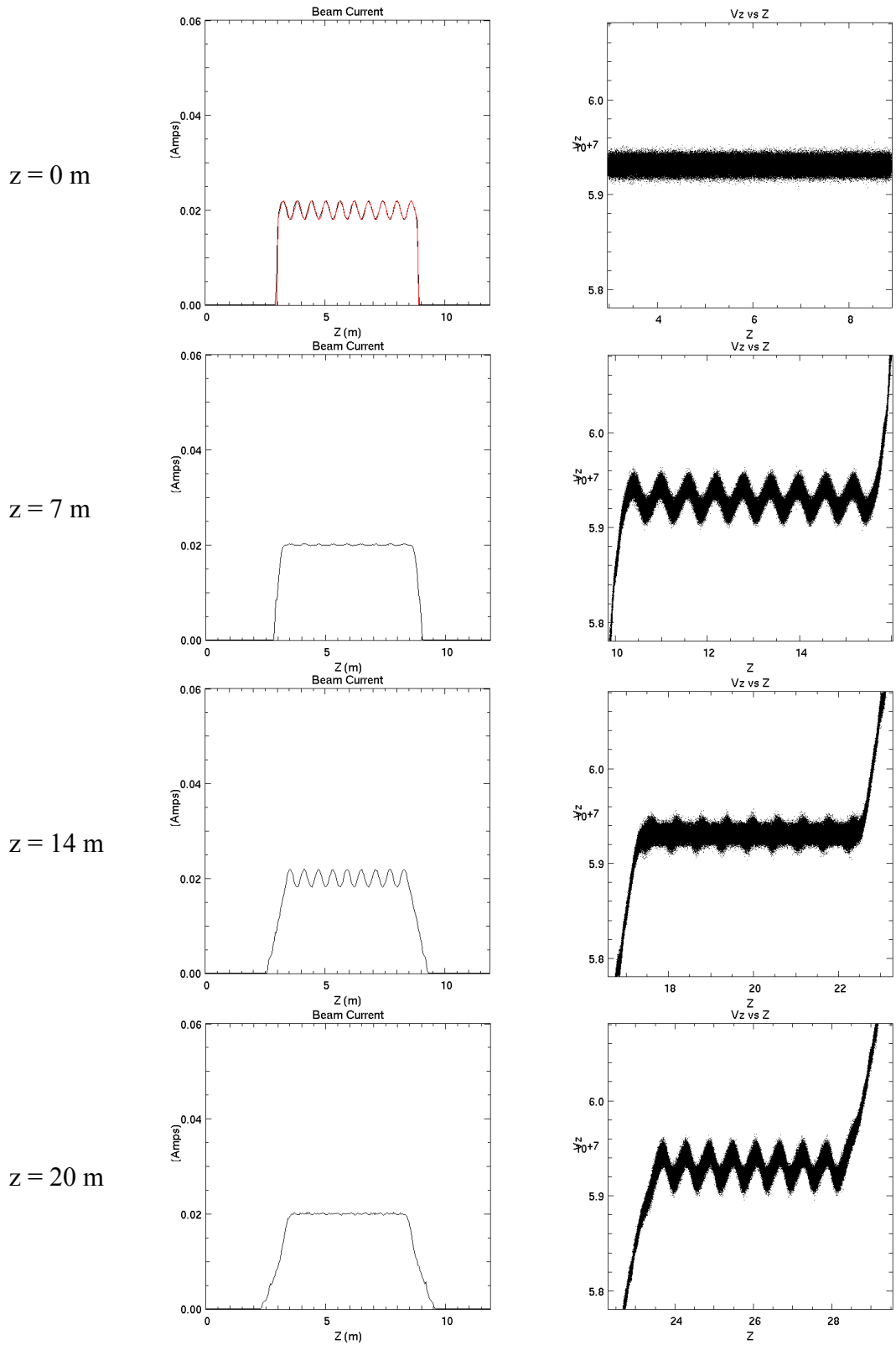
Figure 2.7 The oscillation of density modulation and energy modulation. The left column is current curve and the right column is energy curve.

2.3 Summary

The analytical theory and numerical simulation of longitudinal space-charge waves produced by a pure-density perturbation at the beginning are discussed in this chapter. The sound speed is derived in equation (2.25). Both theoretical and numerical simulation results indicate that initial single pure-density perturbation on a main beam will splits into two peaks. Also, the transformation of the small sinusoid density modulation to the energy modulation is seen in both theory and simulation. The results from WARP 2-D simulation agree with the analytical theory from cold-fluid model.

Chapter 3: Experiments of the Localized Space-Charge Wave

The theoretical analysis and simulation results were studied in Chapter 2. The experiments of the longitudinal space-charge wave are discussed in this chapter.

A brief introduction of the UMER system is presented first. The mechanism of the photocathode is discussed, along with the setup of an ultraviolet laser and the generation of pure-density perturbations. Space-charge waves produced by the pure-density perturbation are studied and current of a special perturbed electron beam is plotted at different position. The sound speeds are calculated for the different combinations of main beam current and perturbation current. The experimental results are compared with the theoretical predictions and the simulation results.

3.1 Experimental Setup

3.1.1 UMER system

Figure 3.1 shows the schematic layout of UMER in May 2004 [23]. The UMER system consists of an electron gun, injection/matching chambers, ring chambers and extraction/diagnostic chamber.

The injection/matching section consists of two straight chambers, IC1 and IC2, shown in Figure 3.2. A large Helmholtz dipole is used to cancel the vertical component of earth magnetic field. This section has 6 quadrupoles, 1 Panofsky quadrupole, 12

steering dipoles and 1 pulsed dipole. All of them are computer-controlled to generate a matched beam for the ring section.

The ring section consists of 18 chambers, RC1 to RC18. The radius of the ring is 1.8 m and circumference is 11.52 m. The detailed specifications of UMER are given in Table 3.1 [24, 25]. Each chamber consists of 2 FODO periods, shown in Figure 3.3. Each FODO period is 32 cm long and consists of two printed-circuit (PC) quadrupoles to confine the electron beam and one PC dipole. The beam is bent about 10 degrees in a FODO period by both the dipole magnetic field and the earth magnetic field. A series of steering dipoles are also used to do the fine adjustment for alignment purpose. Table 3.2 and Table 3.3 give the general design characters for dipoles and quadrupoles [26]. A computer control system built by Dr. H. Li controls all the magnetic components [27]. This system allows a high quality beam by optimizing the beam steering, rotation and matching. Presently, a total of 14 ring chambers have been set up and a very good beam has been achieved at RC12.
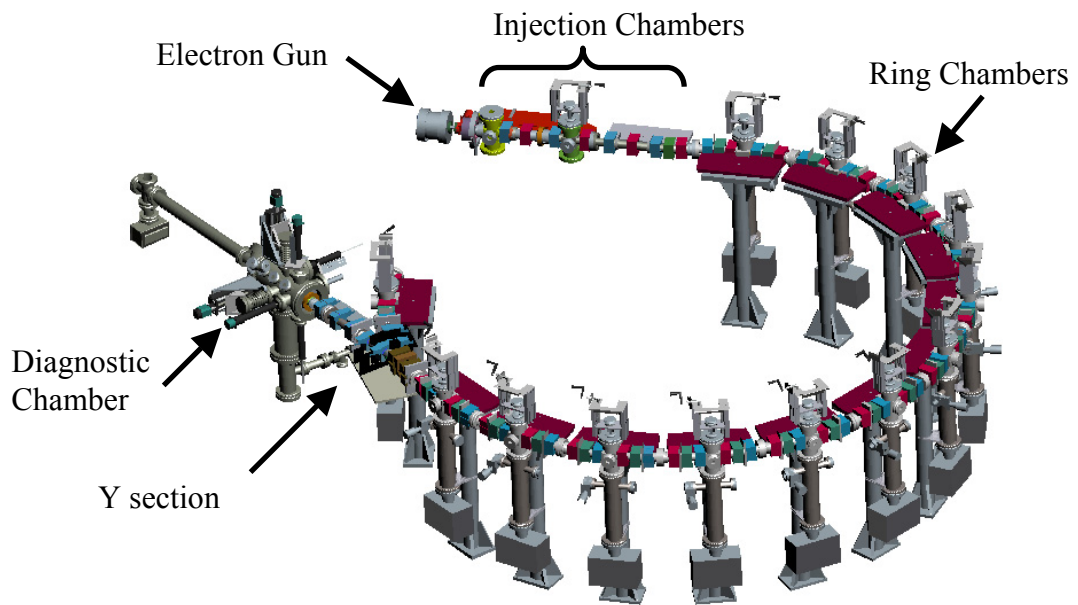
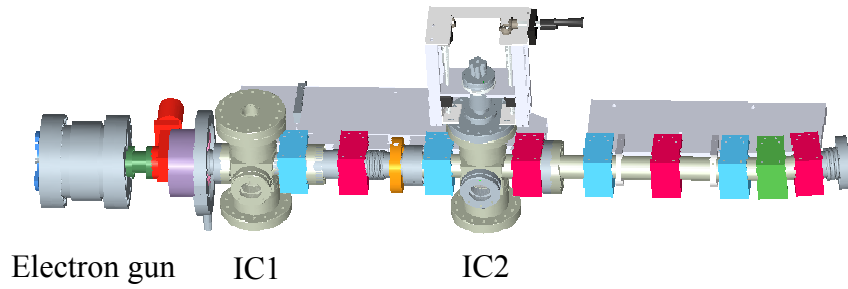Figure 3.1 Layout of Current University of Maryland Electron Ring (UMER)

Figure 3.2 Layout of electron gun and injection/matching section
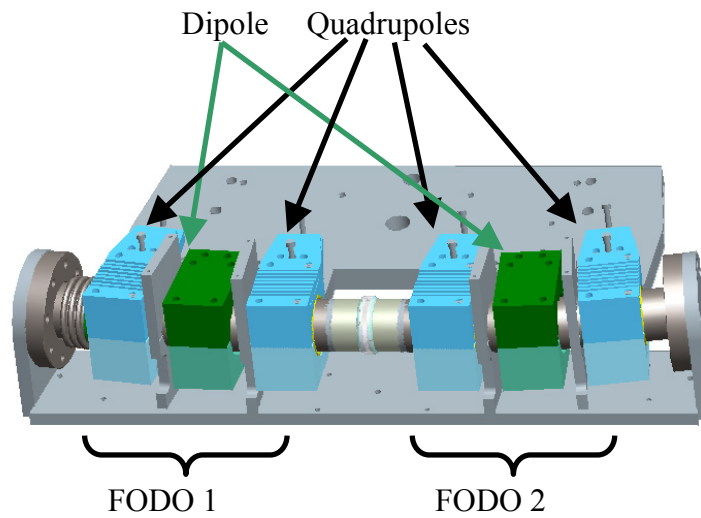
Figure 3.3 Layout of a chamber, two FODO periods (20 degree bend)

Table 3.1 Specifications of UMER for the 10 keV Electron Beam

Energy	10 keV
$\beta(=v/c)$	0.2
Current	100 mA
Generalized perveance	0.0015
Emittance (4*RMS, norm)	10 μm
Pulse length	100 ns
Circumference	11.52 m
Lap time	197 ns
Rep. Rate	10,15,60 Hz
Mean beam radius	<1 cm
FODO period	0.32 m
Phase advance, σ_0	76°
Betatron tune,υ_0	7.6
Tune depression	>0.12

Table 3.2 Design characteristics of the PC dipoles

Dipole field	15.4 G (5.2 G/A)
Current	3 A
Physical length	4.4 cm
Effective length	3.8 cm
Radius	2.8 cm
Field integral	20 Gcm/A
Resistance	3 Ω
Allowed harmonic content	<1%
Transverse alignment error	<0.05 mm

Table 3.3 Design characteristics of the PC quadrupoles

Field gradient	4.1 G/cm/A
Current	2 A
Physical length	4.4 cm
effective length	3.6 cm
Radius	2.8 cm
Field integral	15 G/A
Resistance (room temp.)	7 Ω
Allowed harmonic content	<1%
Transverse alignment error	<0.05 mm

The extraction/diagnostic chamber is connected to the ring chambers by a Y-section shown in Figure 3.4. A pulsed dipole and a Panofsky quadrupole are used to bend the beam 10 degrees left into the extraction chamber or 10 degrees right into the normal ring section. In the diagnostic chamber, several measurement instruments are set up, such as Bergoz Current Transformer, Phosphor Screen, Faraday Cup, Slit-Collector and Pepper-pot mask.

3.1.2 Photocathode on UMER

A standard B-type thermionic dispenser cathode, porous tungsten (W) matrix impregnated with barium calcium aluminate ($6BaO$-$1CaO$-$2Al_2O_3$) with integral filament and grid, was used on UMER. By adjusting the A/K gap, grid voltage and internal pulse-forming cable, a pulse length of 100 ns, current of 100 mA and energy of 10 keV rectangular electron beam is generated. The operating temperature is about 900℃. The photoemission properties of this kind of cathode were studied by B. Leblond in the 1990's [28]. The achieved electron/photon quantum efficiency is 10^{-4}, which is defined as the ratio of the number of photoemission electrons to the number of photons. The similar method is used on UMER to generate a localized longitudinal pure-density perturbation.
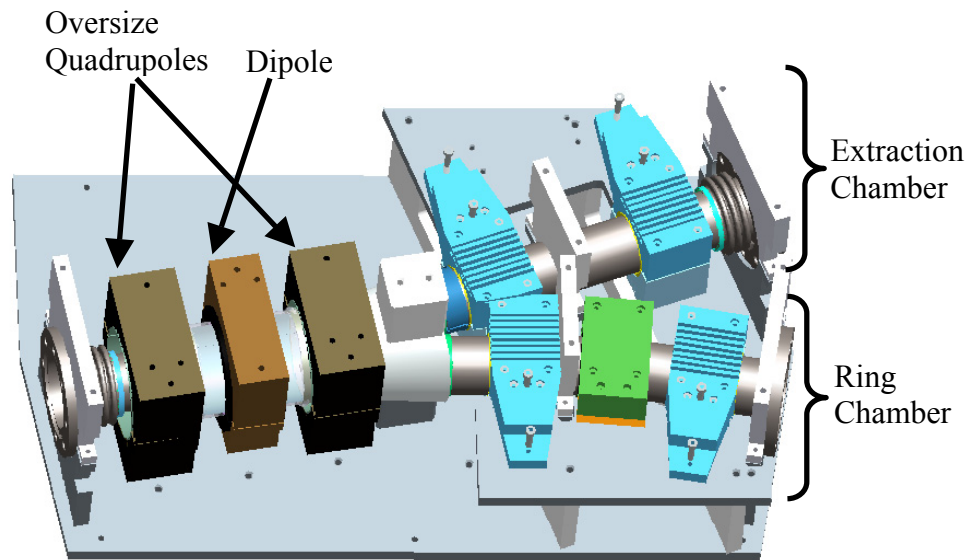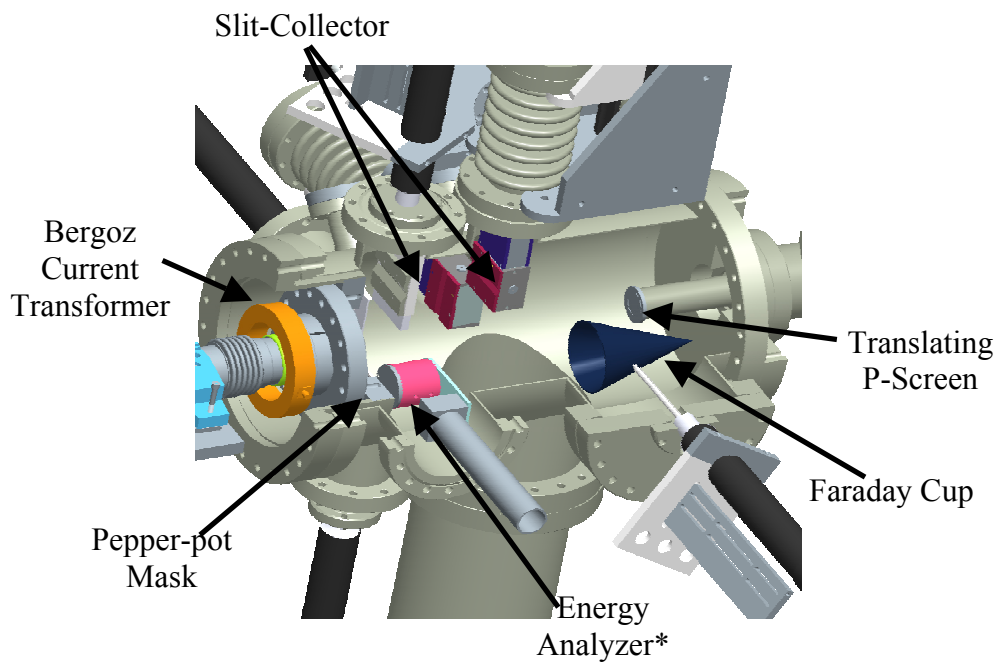
Figure 3.4 Layout of the Y-section

Figure 3.5 Layout of the diagnostic chamber. The energy analyzer will set up soon.

3.1.3 Beam current measurement instruments on UMER

Two kinds of equipment are used to measure the electron beam current: Bergoz Current Transformers and Beam Position Monitors (BPMs). The Bergoz current transformer, model number FCT-082-20:1, is placed at the injection section, 62 cm from the electron gun. The measured rise time of a 25 mA rectangular beam is 2.8 ns.

The BPM is designed to achieve both good spatial and temporal resolution [29]. The upper part of Figure 3.6 shows the schematic layout of a BPM. The rise time is 1.7 ns for a 25 mA rectangular beam at 80 cm from the electron gun. Currently, 13 BPMs are set up at each chamber and the distances from the electron gun to each BPM are listed in Table 3.4.

Table 3.4 The distance between BPMs and the end of electron gun

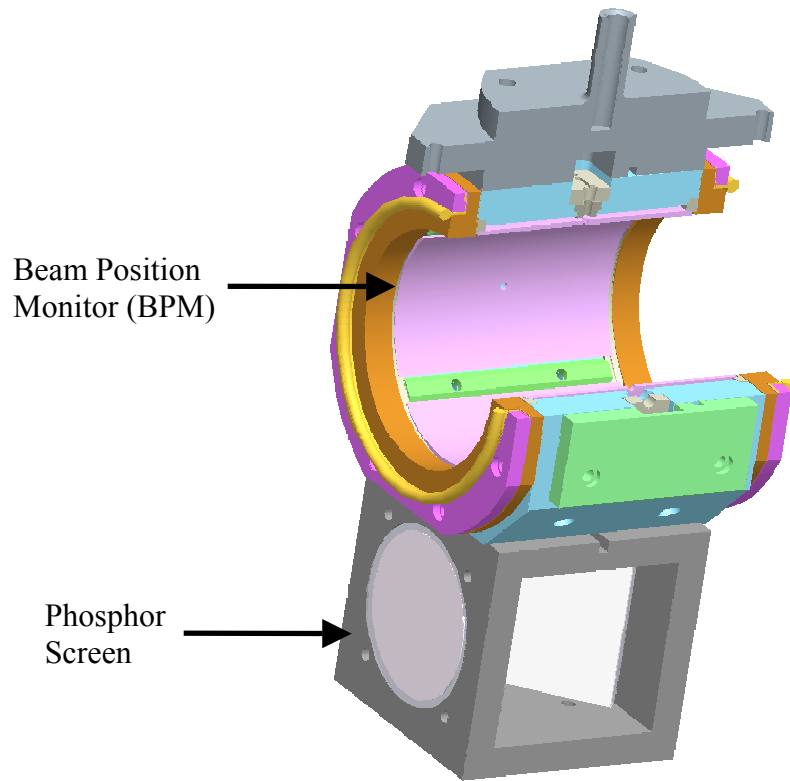|	
Window : IC1	0.36 m
Bergoz current transformer	0.62 m
BPM : IC2	0.80 m
BPM : RC1	1.91 m
BPM : RC2	2.55 m
BPM : RC3	3.19 m
BPM : RC4	3.83 m
BPM : RC5	4.47 m
BPM : RC6	5.11 m
BPM : RC7	5.75 m
BPM : RC8	6.39 m
BPM : RC9	7.03 m
BPM : RC10	7.67 m
BPM : RC11	8.31 m
BPM : RC12	8.95 m

Beam Position Monitor (BPM)

Phosphor Screen

Figure 3.6 Layout of the Beam Position Monitor (BPM) and phosphor screen

These two kinds of equipment associated with the HP Infinium Oscilloscope (Agilent Models 54846B), with sampling rate of 8 GSa/s, give the time evolution of electron beam current at different positions with a 0.25 ns time resolution.

3.1.4 Phosphor screen on UMER

Fourteen phosphor screens, shown in the low part of Figure 3.6, are set up in all the existing chambers. The cross-section beam distribution is shown by phosphor screen and sent to a computer through CCD camera to calculate the beam center, radius, and rotation. With a computer controlled optimization program, a 25 mA good quality beam can be achieved and shown in Figure 3.7 [27].

3.2 Pure-density perturbation generation

3.2.1 Physical concept of photocathode

Figure 3.8 shows the mechanism of the photoemission beam generation. The thermionic 100 ns, 108 mA electron beam current is generated without using drive laser. In thermionic mode, the cathode operates at $900℃$, and the electron gun runs in the space-charge limited region. A thermionic emission electron beam with lower current is generated when the cathode works at lower temperature, shown in Figure 3.9(a). If a laser beam with proper wavelength shines on the cathode, many photoemission electrons are generated at the photocathode and form a short current spike, shown in Figure 3.9(b). When the cathode temperature is below the threshold temperature of thermionic emission, only photoemission current remains. The photoemission electron beam current is shown in Figure 3.9(c).
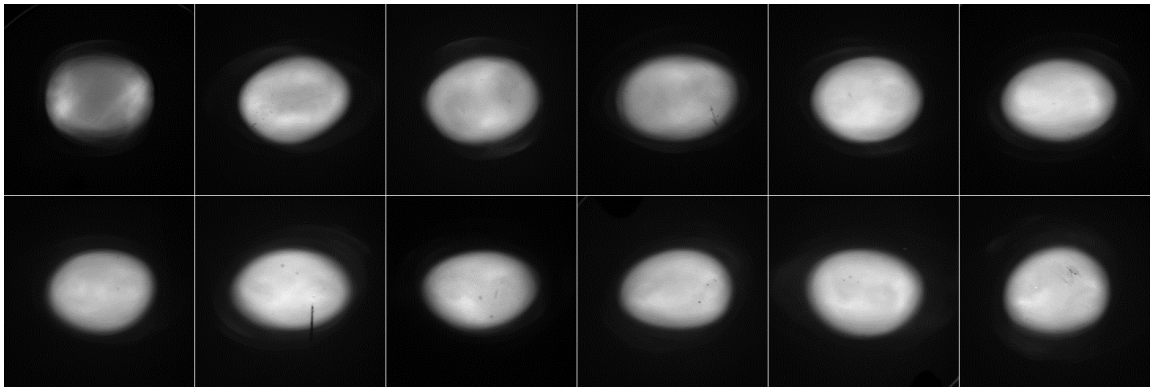
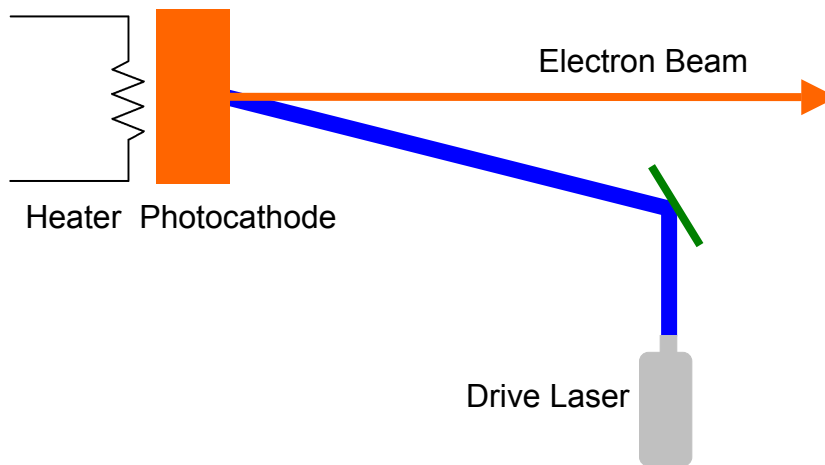Figure 3.7 Transverse distribution of 25mA electron beam
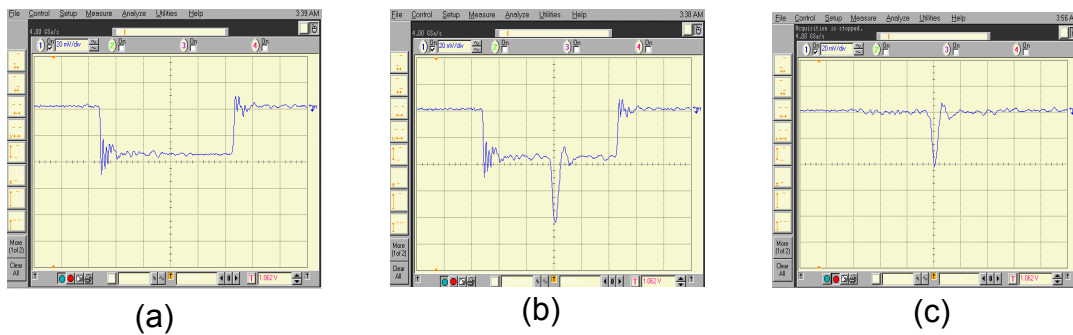

Figure 3.8 Schematic for photoemission mechanics

Figure 3.9 Beam current measured by Bergoz current transformer. (a) 100 ns thermionic emission electron beam only, (b) combination of photo and thermionic emission electron beam, (c) 5 ns photoemission electron beam only.

3.2.2 Drive laser setup and pure-density perturbation generation

Figure 3.10 shows the schematic layout of the drive laser for photoemission beam generation. A Minilite Q-Switched Nd:YAG laser is used as the laser source [30]. The wave length of this laser is 1064 nm; the maximum pulse power is 50 mJ; the peak power is 8.3 MW; the full width at half magnitude (FWHM) of the laser pulse is about 5 ns and the repetition rate is 10 to 15 Hz. A second-harmonic crystal, Potassium Titanium Oxide Phosphate ($KTiOPO_4$, KTP) crystal, is used to generate a green laser at 532 nm, whose maximum pulse power is 25 mJ. Then a beta-BaB_2O_4 (BBO) crystal is used to generate an ultraviolet laser at 355 nm, whose maximum pulse power is 8 mJ. The ultraviolet laser is reflected by two high power dielectric mirrors. These mirrors also act as a filter system, whose center-wave of reflection is 355 nm. The high intensity (small cross section) ultraviolet laser beam is expanded by a telescope in order to illuminate the entire cathode. A laser mask may also be used to modulate the laser beam transversely. With three more mirrors and one mirror in the first injection chamber (IC1), a pure ultraviolet (355 nm) 5 ns laser pulse impinges on the cathode to generate the photoemission electrons. An ultraviolet laser is chosen since the higher photon energy gives higher quantum efficiency. The same amount of photoemission current is generated with a low power ultraviolet laser or a high power green laser. Pictures of drive laser and mirror in IC1 are shown in Figure 3.11 and Figure 3.12.

The flash lamp of the Nd:YAG laser is triggered by a pulse generator at 10Hz or 15Hz repetition frequency. The pulse width of flash lamp output is about 250 μs. About 150 μs after the flash light triggers on, the Q-switch triggers, and about 60 ns later a laser pulse is generated with FWHM of 5 ns. The Q-switch trigger pulses also trigger the

electron gun to generate an electron bunch with 100 ns pulse width. As a result, a pulse width of 5 ns photoemission current is generated at the center of a 100 ns rectangular main beam, which is shown in Figure 3.9(b).

Laser Mask

Telescope

Mirrors/filters

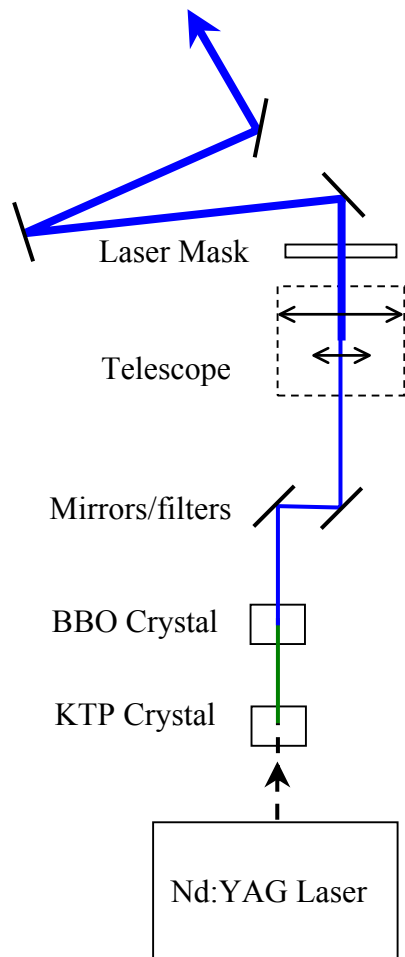BBO Crystal

KTP Crystal

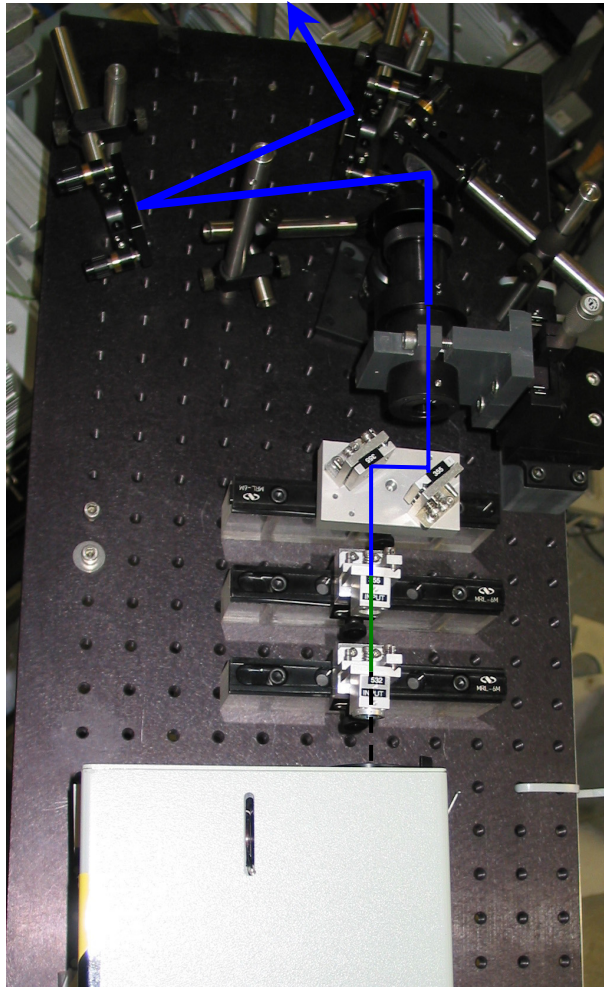Nd:YAG Laser

Figure 3.10 Schematic layout of drive laser

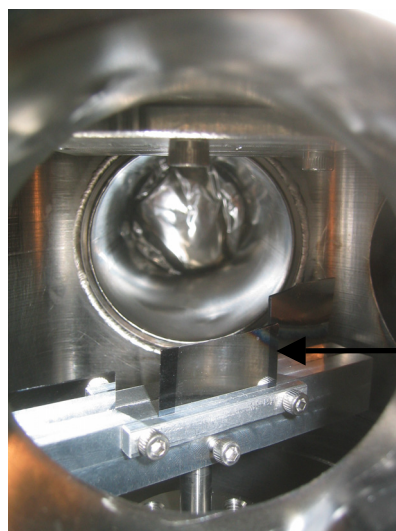Figure 3.11 Picture of drive laser

Figure 3.12 Picture of mirror in the first injection chamber (IC1)

The photon energy of the ultraviolet laser (355 nm) is 3.50 eV. Under normal thermionic emission condition, the work function of the cathode material is minimum, $W_{\Phi th} \approx 2$ eV [31]. When the temperature decreases, $W_{\Phi th}$ increases to approach the value $W_{\Phi th} \approx 2.7$ eV of Ba. This means that the energy spread of the photoemission electrons is less than 0.8 eV. The energy spread of the main beam electrons at the end of the electron gun is usually 1 eV, larger than photoemission energy spread (0.8 eV). The final energy modulation, which is produced by the initial density perturbation, is several tens of electron volts, which is much larger than 0.8eV. Also consistent with previous work, the grid voltage induced perturbation is several tens of electron volts. So the energy distribution of the photoemission electrons is almost the same as that for thermionic emission electrons.

The relationship between the electron beam current I, the longitudinal line charge density Λ and the velocity of the electrons v is $I = \Lambda*v$. The same energy distribution for both photoemission electrons and thermionic emission electrons yield the same velocity distribution for all electrons. So the current modulation is only due to the modulation of the longitudinal line charge density.

In conclusion, this laser produced current perturbation is a localized longitudinal pure line charge density perturbation. The following experiments examine the space-charge wave behaviors of this localized density perturbation on a 100 ns main beam.

3.3 Experiments on localized longitudinal space-charge wave

3.3.1 Typical example from experiments

Before the general discussions of the space-charge wave behaviors of the pure-density perturbation, a typical case (with 20 mA 100 ns main beam and 20 mA 5 ns perturbation) is presented first. A 20 mA perturbation beam is chosen since it is easier to see the evolutions of the perturbation, although the nonlinear effects are also important here.

Figure 3.13 shows the beam current measured at a Bergoz current transformer at 62 cm from the electron gun. This electron bunch transports through 12 ring chambers. Beam current is measured by BPMs at each chamber, shown in Figure 3.14. All the current signals are normalized to allow the main beam current to read unity.

From RC1 to RC5, 191 cm to 447 cm from electron gun, the pure-density perturbation spreads wider and wider due to the space-charge force. At RC6, 511 cm from the beginning, the perturbation splits into two peaks. Then these two peaks, called two space-charge waves, keep moving away from each other. This longitudinal space-charge wave behavior is the same as the prediction from theory and simulation in Chapter 2.

In order to show the evolution of the perturbation clearly, perturbation current is calculated by subtracting only the thermionic contribution from the total beam current, which includes both photoemission and thermionic emission electrons. This calculation is shown in Figure 3.15. The perturbation current is calculated at each chamber in a similar way and results are shown in Figure 3.16.
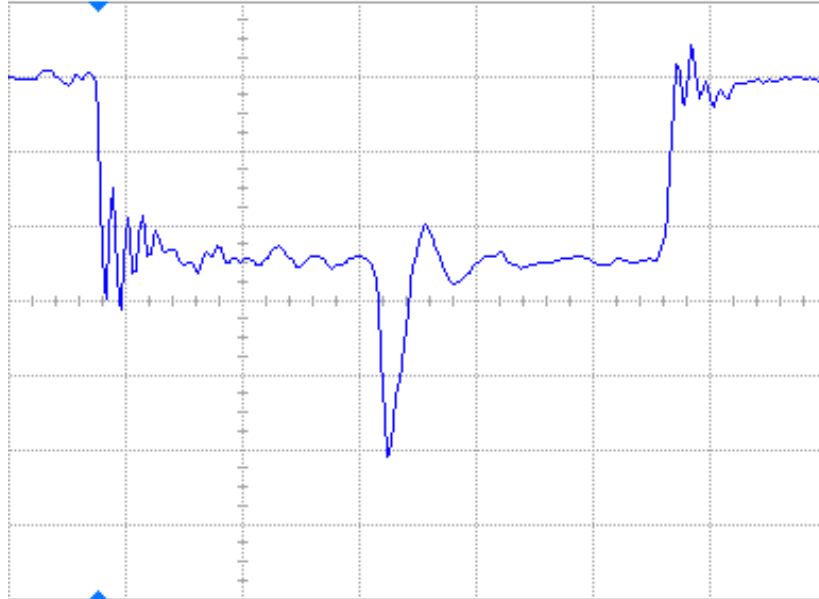
Figure 3.13 The current for the perturbed electron beam at 62cm from the electron gun
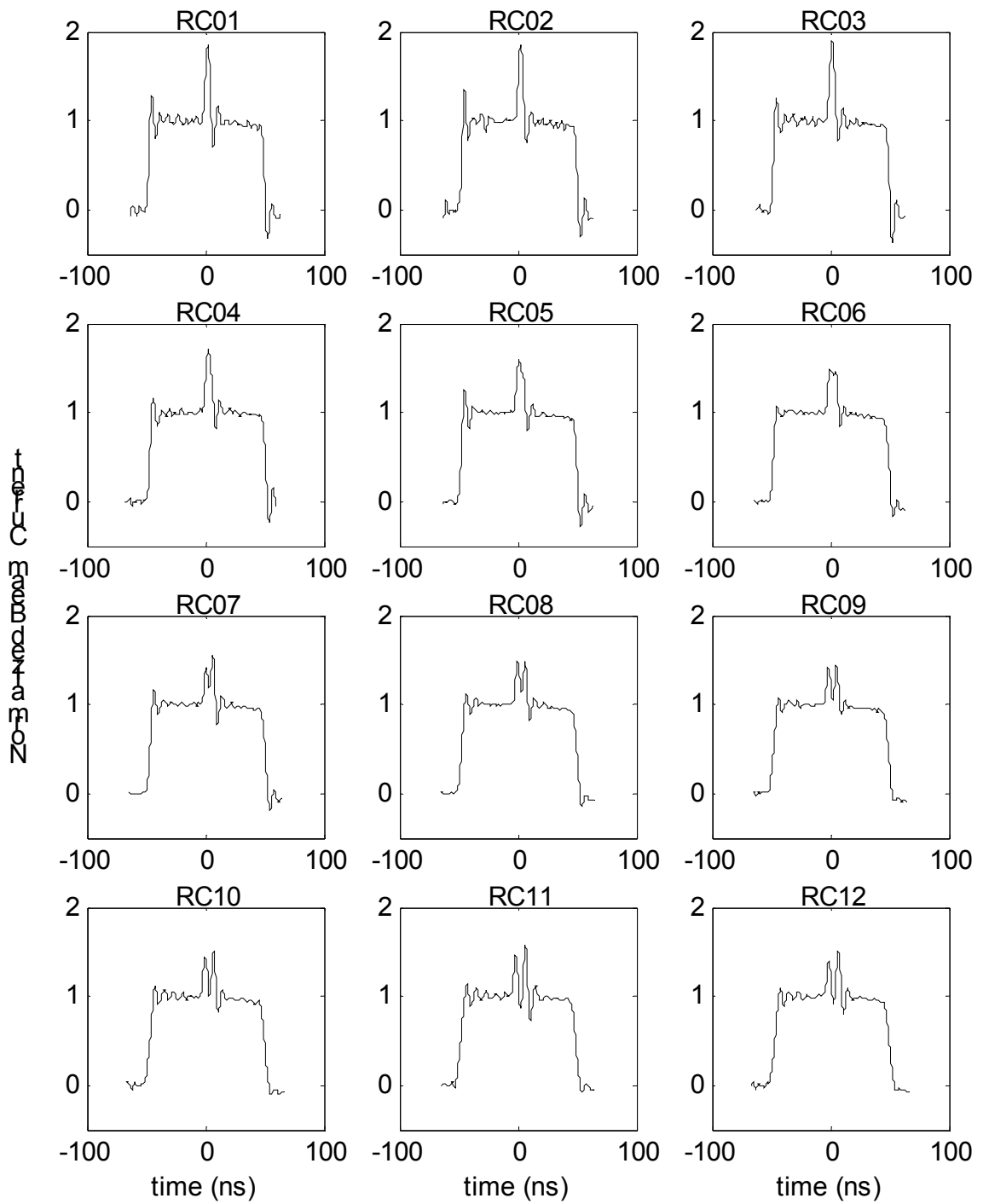
Figure 3.14 Evolution of perturbed electron beam, 20mA main beam current and 20mA perturbation current at the beginning.
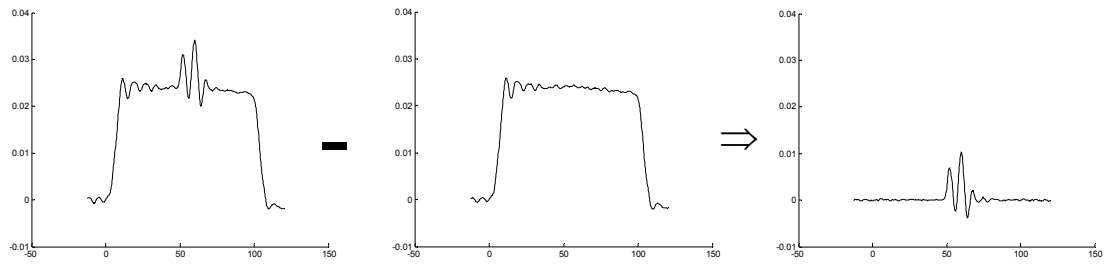
Figure 3.15 Example perturbation current calculation
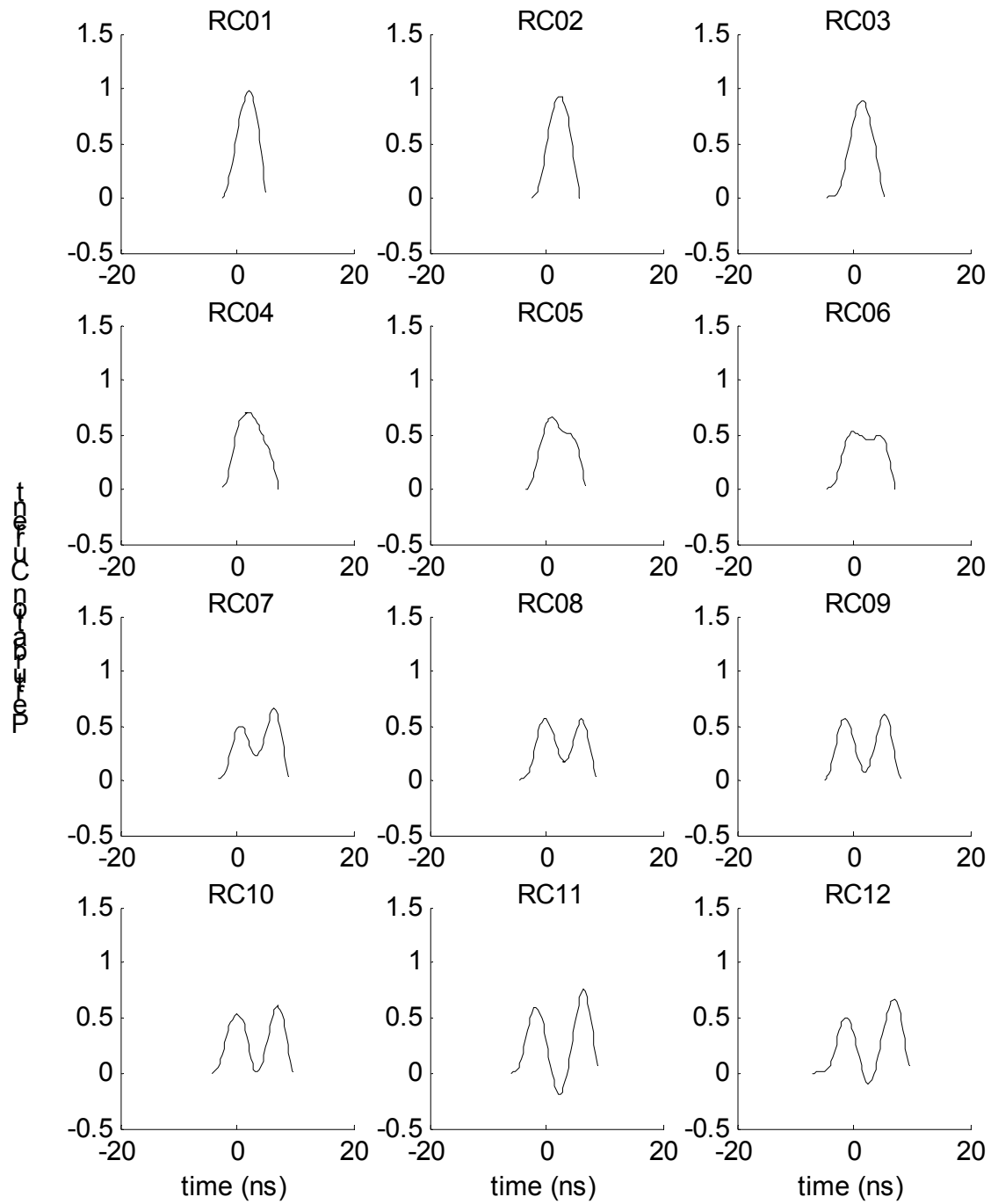
Figure 3.16 Evolution of perturbation (subtracted by main beam current)

In Figure 3.16, the shape of the head of the fast space-charge wave and the tail of the slow space-charge wave do not change from the beginning to the end. The same results are obtained via simulation.

According to theoretical discussions in Chapter 2, these two longitudinal space-charge waves travel at twice of sound speed C_s leave away from each other. The time spans between these two peaks are plotted in Figure 3.17. Since each BPM has four channels, four slightly different span times arrive at each position, each represented by a blue star in the graph. The mean value of the four span times at each position is calculated and showed by a red circle. A line is fitted for these mean time spans by using the least square root method. Speed of sound can be calculated by using,

$$2*C_s = \frac{\Delta(\text{Distance between two peaks})}{\Delta T} = \frac{\Delta t \cdot v}{\Delta z / v} = \frac{\Delta t}{\Delta z}(\beta c)^2 \tag{3.1}$$

where Δt is the time increase between two peaks when the beam travel for Δz meters, and $\Delta t / \Delta z$ is also the gradient of the fitting line. From Figure 3.17 and equation (3.1), one can calculate the sound speed from experimental data, $C_s = 1.38*10^6$ m/s.
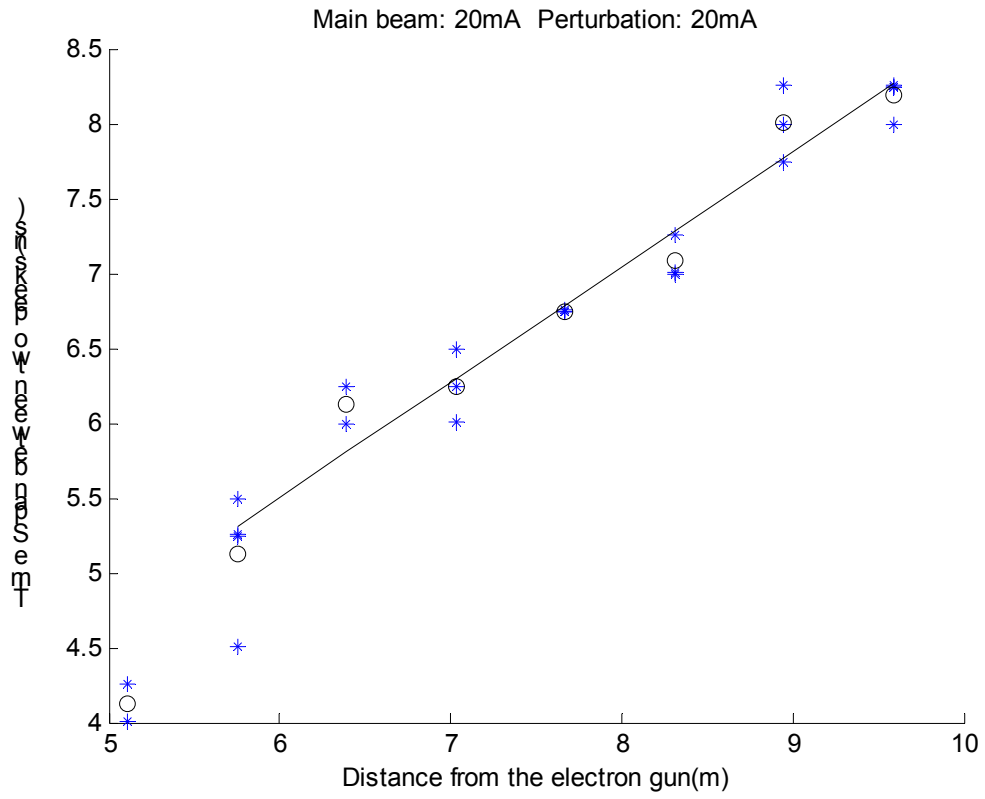
Figure 3.17 The separation times between two current spikes at different positions

In order to calculate the sound speed C_s from equation (2.25) in theory, the beam radius must be calculated first. There are two ways to arrive at beam radius: one way is to calculate the match beam radius for the FODO period from envelope equation; the other way is to use transverse beam distribution figures from the phosphor screens at each chamber to calculate the mean radius. Figure 3.18 shows transverse beam distributions from RC1 to RC11. The RMS beam radius at each chamber is measured and averaged. The mean value of the beam radius is 0.4 cm. Setting a = 0.4 cm in equation (2.25) with b = 2.54 cm, Λ = I/v = 3.33*10^{-10} C/m, the sound speed is equal to 1.26*10^6 m/s. The result from experiments is therefore larger than the theoretical prediction. This is because in theory, a small modulation is assumed. However, in this example experiment, a huge perturbation, the same amplitude as the main beam, is used. The nonlinear effects of strong space-charge force make the two peaks separate at a higher speed.

RC1   RC2   RC3

RC4   RC5   RC6

RC7   RC8   RC9

RC10   RC11

Figure 3.18 Transverse beam distributions from phosphor screen at RC1 to RC11

3.3.2 Experiments of different main beam current and perturbation current

A 20 mA 5 ns perturbation on the 20 mA 100 ns main beam is discussed in the previous section. The initial single density pertur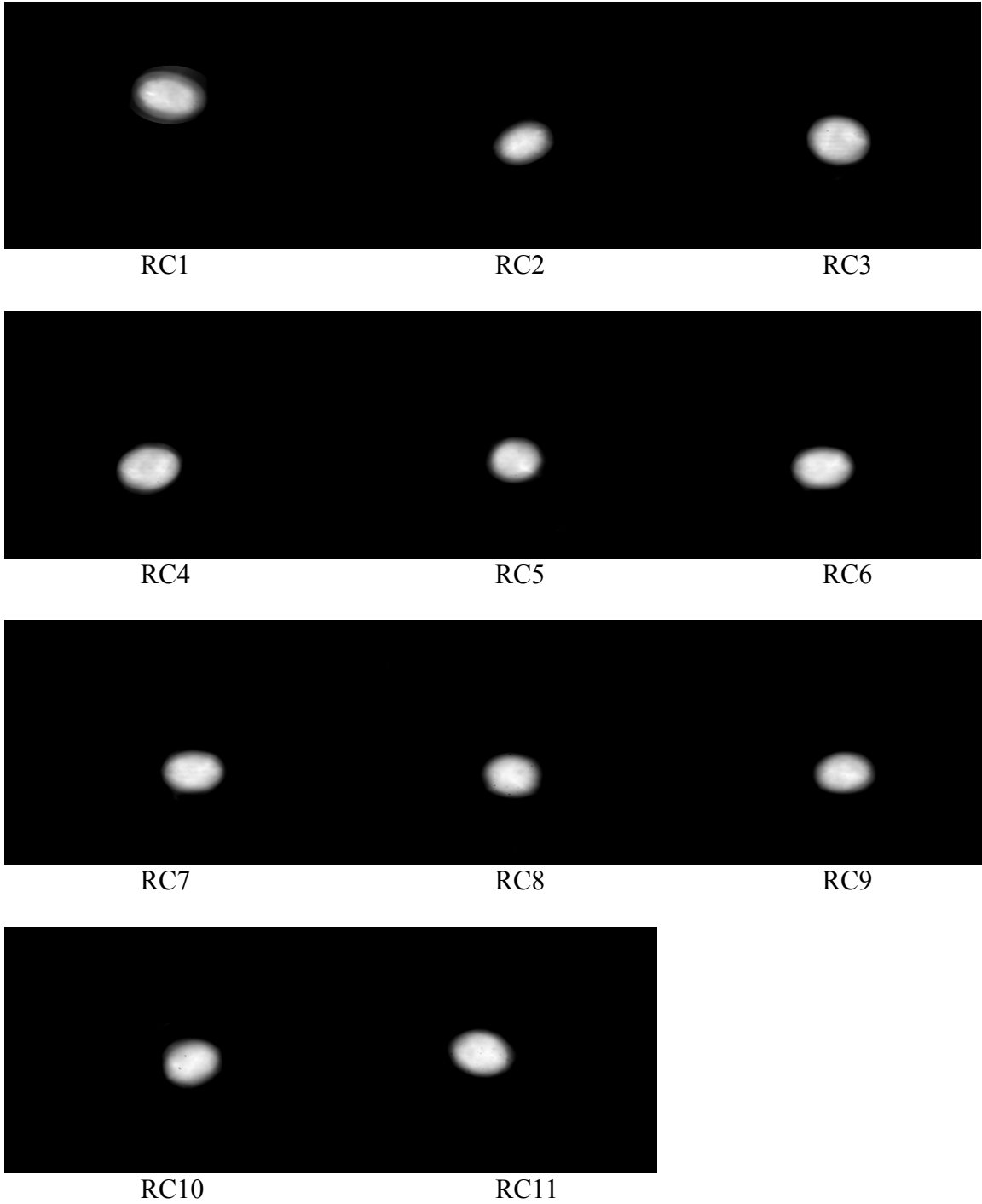bation generates two space-charge waves, one fast wave and one slow wave. The relative speed between the two space charge waves is equal to twice the sound speed, where $C_s=1.38*10^6$ m/s. Some different combinations of main beam current and perturbation current are discussed in this section to study the space-charge wave characteristics.

First, the change of sound speed is considered for the same perturbation on the different main beams. In order to eliminate the nonlinear effects, an 8 mA 5 ns perturbation is studied in this set of experiments. The main beam current is changed to 20 mA, 37 mA, 50 mA, 65 mA, and 80 mA, respectively. The evolutions of the electron beam current at the beginning and end are shown in Figure 3.19.

As discussed in previous section, the sound speed is calculated for each case and presented by squares in Figure 3.20. The sound speed also can be calculated from equation (2.25) and plotted in Figure 3.20 by triangles. The results are listed in Table 3.5. The radius for different main beam is calculated by a match code, MENV [27], and listed in Table 3.6. The difference of beam radius between the simulation and experiment is about 10%, resulting in about 3% difference for the sound speed calculation.
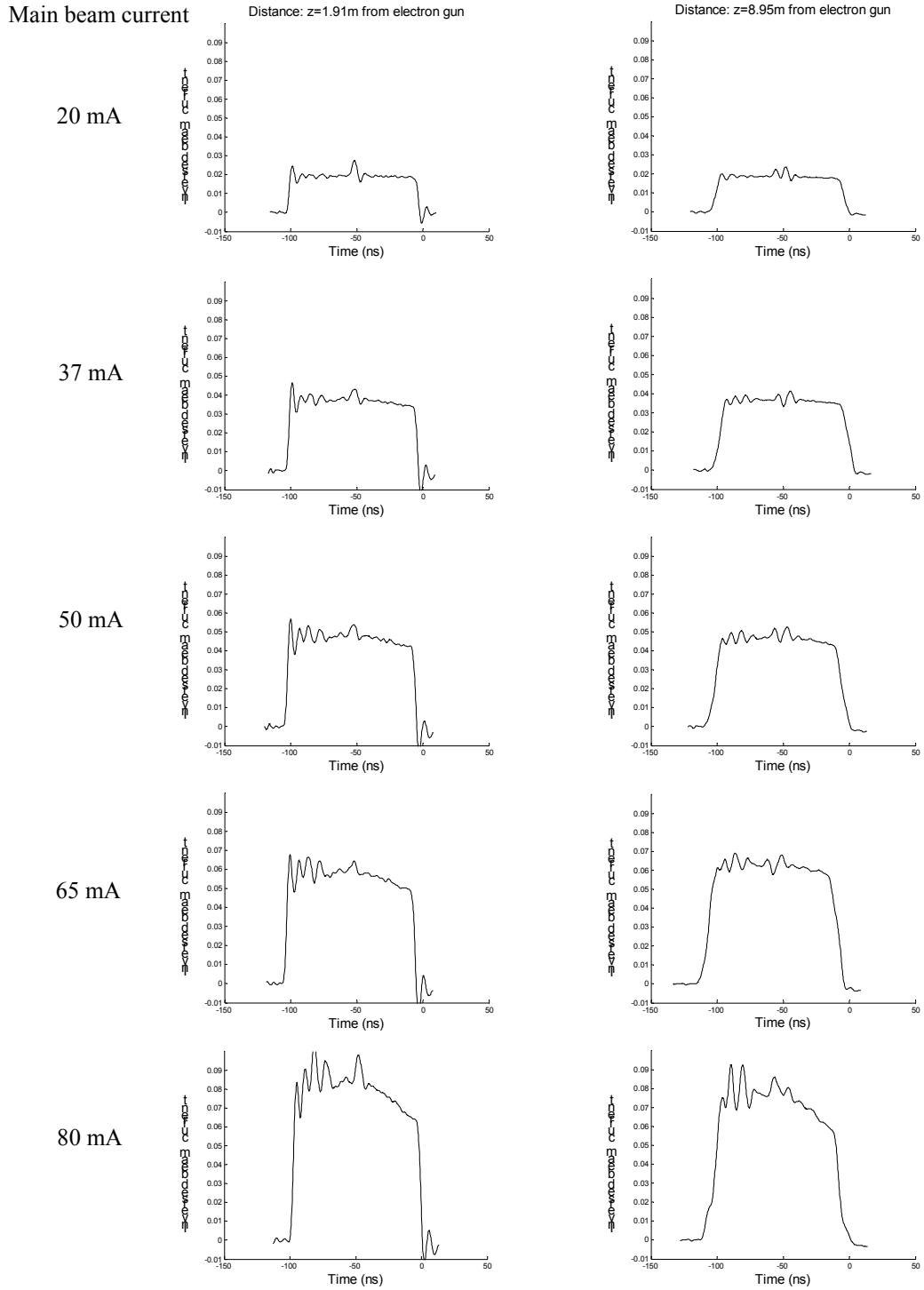
Figure 3.19 The beam current for different main beam current and same perturbation current at beginning and ending of electron ring. The main beam current is 20 mA, 37 mA, 50 mA, 65 mA, 80 mA, respectively.
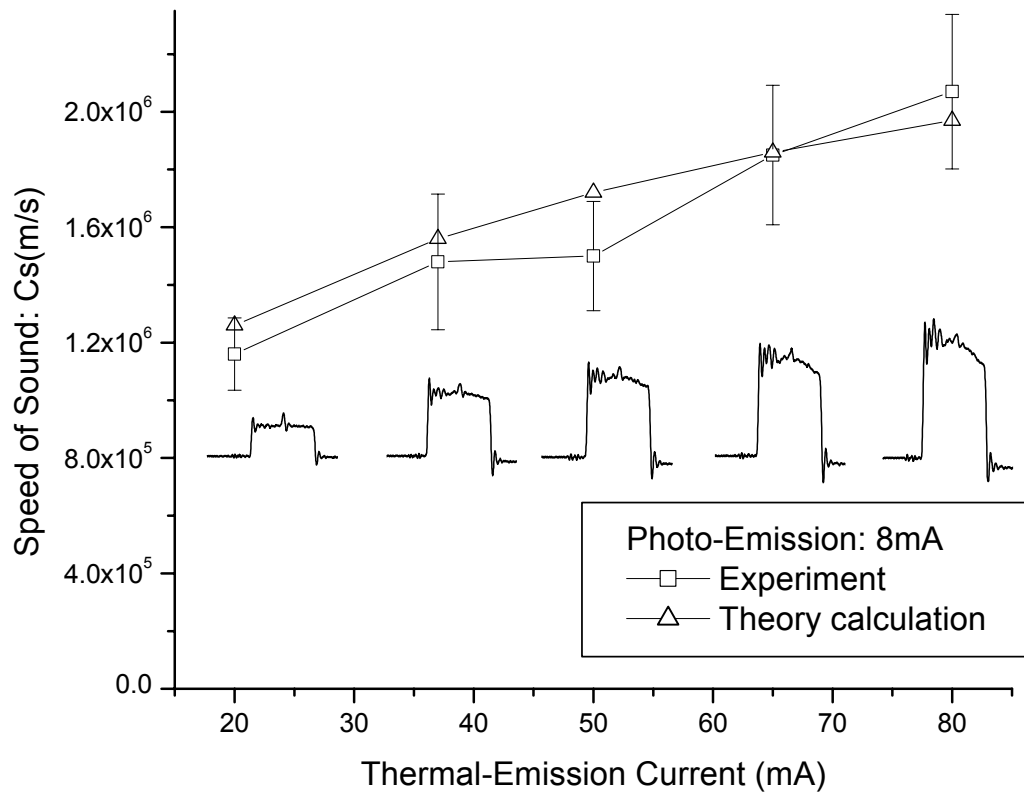
Figure 3.20 The sound speed for same initial perturbation with different main beam current. The squares in the figure represent the sound speed measured by the experiment. The triangles in the figure represent the sound speed calculated by the theory.

Table 3.5 The sound speed calculation for different main beam current

	Main beam current (mA)	Perturbation current (mA)	Cs (m/Sec) (Experiment)	Cs (m/Sec) (Theory)
1	80	8	2.07E+06	1.97E+06
2	65	8	1.85E+06	1.86E+06
3	50	8	1.50E+06	1.72E+06
4	37	8	1.48E+06	1.56E+06
5	20	8	1.16E+06	1.26E+06

Table 3.6 Beam radius for different current beam

Main beam current (mA)	Mean Beam radius (mm)
20	4.624
37	6.137
50	7.076
65	8.022
80	8.868

In Figure 3.20, the sound speed is increasing when the main beam current is increasing. This result agrees with the theoretical prediction. Since in the equation (2.25), the sound speed is proportional to the square root of main beam line charge density. This phenomenon is similar to sound wave propagation in different media such as air, liquid or solid. The only difference is that sound waves are formed by the molecular vibrations produced by recovery force, while space-charge waves are formed by the electron vibrations produced by space-charge force. For sound waves, the wave traveling speed in a solid material is faster than that in liquid, and the speed in liquid is faster than that in gas. The same is true for longitudinal space-charge wave, the sound speed is faster in a larger current main beam. The main beam is very important because it gives a medium that permits the space-charge wave propagation. In contrast, Figure 3.21 shows the

evolution of a parabolic electron beam in UMER without a main beam. The parabolic electron beam only spreads in the first 12 ring chambers without splitting into two bunched electron beams like the perturbation discussed in this chapter.

Distance: z=0.80m from electron gun

Distance: z=8.95m from electron gun
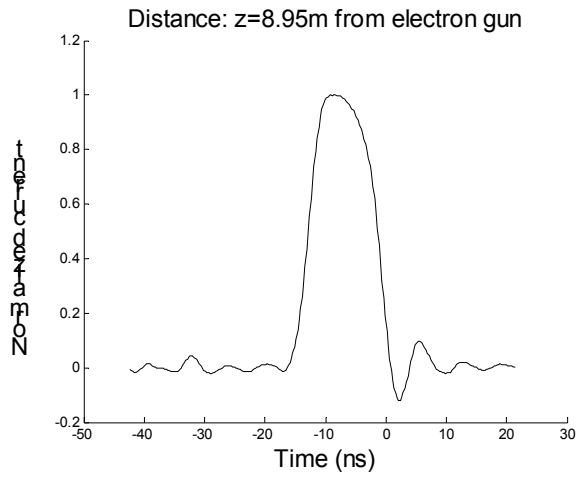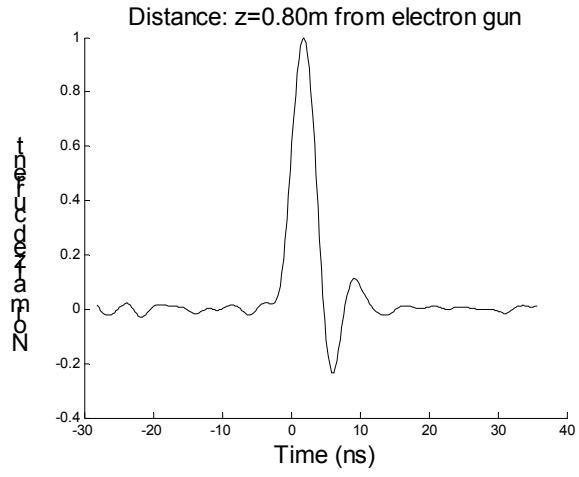
Figure 3.21 The spread of a parabolic beam (no split)

Considering the second set of experiments, the same 20 mA 100 ns main beam is used with different perturbations at 8, 14 and 20 mA, respectively. The evolution of these electron beams is plotted in Figure 3.22. The sound speed of the space-charge wave is calculated and plotted in Figure 3.23. The results are also shown in Table 3.7. Since the main beam current doesn't change, the sound speed calculated from the equation (2.25) doesn't change. However, in the experiment, the sound speed is increasing while the perturbation is increasing. This is due to the nonlinear effects, which is not included in the theoretical analysis. In the 20 mA perturbation case, the magnitude of the perturbation is same as the main beam current, and the nonlinear effects seriously impact the beam propagation. The larger space-charge force pushes the two perturbations apart at faster than twice of sound speed calculated from the theory. Some interesting longitudinal instability phenomena in nonlinear region were also found in Dr. Y. Zou's experiment [16]. Up to now, no theory gives good prediction in the nonlinear region.
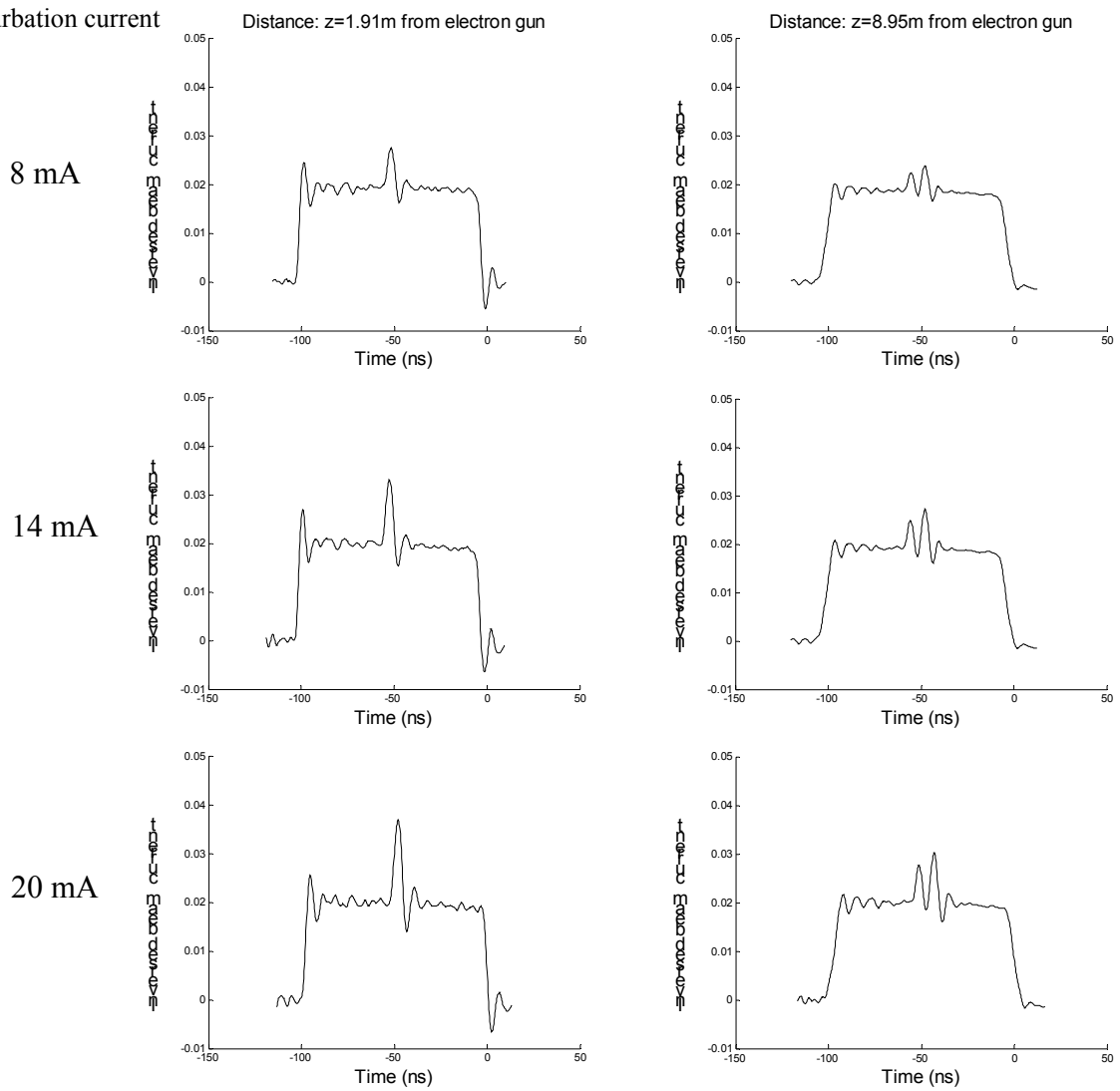
Figure 3.22 Beam current for same main beam current and different perturbation current at beginning and ending of the electron ring. The perturbation current is 8 mA, 14 mA and 20 mA, respectively.
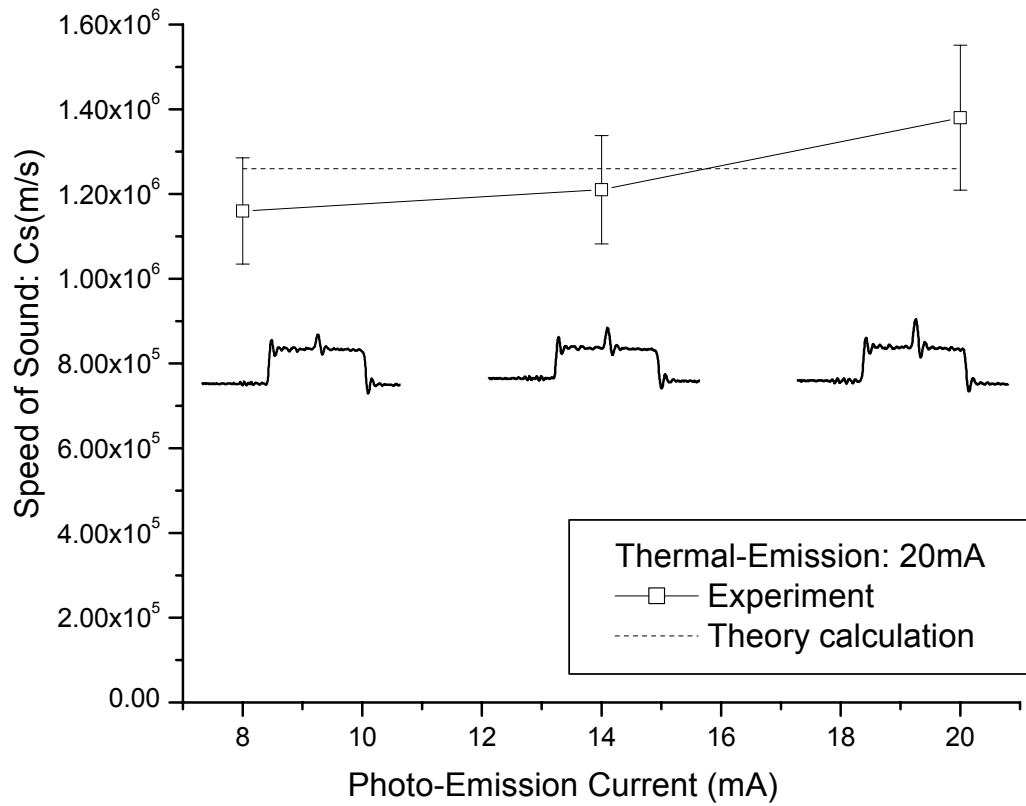
Figure 3.23 The sound speed for different initial perturbation current with same main beam. The squares in the figure represent the sound speed measured by the experiment. The dashed line in the figure represents the sound speed calculated by the theory.

Table 3.7 The sound speed calculation for different perturbation currents

	Main beam current (mA)	Perturbation current (mA)	Cs (m/Sec) (experimental)	Cs (m/Sec) (Theory)
1	20	8	1.16E+06	1.26E+06
2	20	14	1.21E+06	1.26E+06
3	20	20	1.38E+06	1.26E+06

3.4 Summary

In this chapter, the propagation of laser produced longitudinal single-density perturbation in space-charge dominated beam was discussed. Several important points are worth noting:

1. A drive laser table is set up by using the Nd:YAG laser. A third harmonic ultraviolet pulse laser (5 ns, 8 mJ, and 355nm) is produced and impinged on the entire cathode.

2. The photoemission current in UMER is observed. The different current combinations of 100 ns main beams and 5 ns density perturbations are generated and propagate through 12 chambers of UMER.

3. The initial single-density perturbation splits into two space-charge waves. The two space-charge waves separate from each other at twice the sound speed.

4. The sound speed of the space-charge wave increases with main beam currents, similar to the sound wave propagation at different speeds in gases, liquids and solids.

5. The sound speed increases when the perturbation is larger at a constant main beam current due to the nonlinear effects.

6. The sound speed observed from experiments agrees well with the theoretical predictions and simulation results.

Chapter 4: Preliminary Experimental Study of the Transverse Phase Space Tomography for Photoemission Electron Beam

4.1 Introduction

4.1.1 Introduction to tomography

The original definition of Tomography refers to the cross-sectional imaging of an object from either transmission or reflection data collected by illuminating the object from many different directions. The mathematical fundamental is developed by Radon in 1917 [32]. Hounsfield used this method to invent the x-ray computed tomographic scanner to form images of tissues and received the Nobel Prize in 1972. This technique is called Computerized Tomographic Imaging, or CT imaging for short. The methods of computerized tomography are also used in numerous non-medical imaging applications, such as the mapping of underground resources, cross-section imaging for nondestructive testing, the calculation of the brightness distribution over a celestial sphere, and three-dimensional imaging with electron microscopy. Recently, the technique of computerized tomography is also used in beam physics to reconstruct the transverse phase space [33] the longitudinal phase space [34], and to measure the emittance of beam [35].

4.1.2 Prior Research

The tomography technique is also applied to UMER to reconstruct the transverse phase space and to calculate the beam emittance. The quadrupole current-control program and the transverse phase space reconstruction program are designed by Dr. H. Li. The

transverse phase space of a 0.6 mA 100 ns rectangular electron beam is reconstructed and

shown in Figure 4.1 [27]. Since the beam current is only 0.6 mA, a linear propagation

matrix can be used in the calculation. The unnormalized 4*RMS (effective) emittance of

the beam is also calculated, $\varepsilon_x = \varepsilon_y = 5.5$ mm-mrad. The pseudo color is used to show the

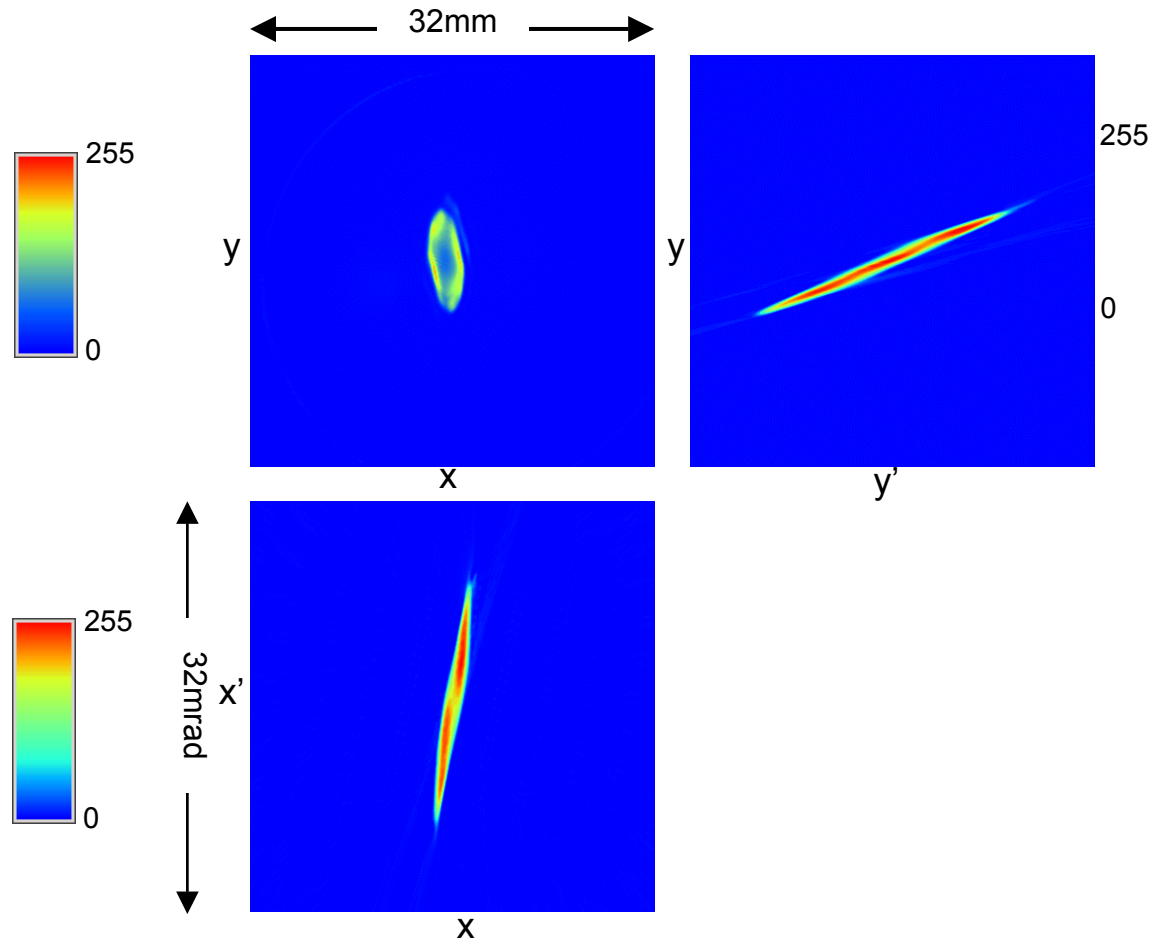detailed structures inside the beam.

Figure 4.1 Phase spaces of a 0.6 mA beam at RC1, 191cm from electron gun. The y vs. x figure is the beam cross-section distribution. The x' vs. x figure is the phase space in x direction. The y' vs. y figure is the phase space in y direction.

4.2 Tomography of the photoemission electron beam on UMER

The photoemission electron beam in UMER is very useful. However, only a few beam characteristics are known about this beam. The computerized tomography can be used in this kind of electron beam to reconstruct the transverse phase space of the electron beam and to calculate the emittance, which is very important for the future experiment.

The Radon transform of a function f(x,y) is defined as the line integrals for all the directions, [27]

$$r(p,\phi) = R \bullet f(x,y) = \int_L f(x,y)ds, \tag{4.1}$$

where the line integral is along the line $p = x\cos\phi + y\sin\phi$ $(0 \le \phi \le \pi)$. The inverse transform can be written as

$$f(x,y) = R^{-1} \bullet r(p,\phi) = \int_0^\pi \tilde{r}(x\cos\phi + y\sin\phi, \phi)d\phi, \tag{4.2a}$$

$$\tilde{r}(s,\phi) = F^{-1}\left[|k| \cdot F\left[r(p,\phi)\right]\right], \tag{4.2b}$$

where $\tilde{r}(s,\phi)$ is a modified projection function, F and F^{-1} are one-dimensional normal and inverse Fourier transform. Here, the $r(p,\phi)$ is the projection function, which is given by

$$r(p,\phi) = s \cdot C(l,\phi), \tag{4.3}$$

where $C(l,\phi)$ is the beam profiles in x or y direction, which can be calculated from the experiment. The scaling factor s and phase space rotation angle ϕ can be calculated for different quadrupole currents.

In order to obtain the transverse phase space, the profile data for all 180 degree phase space rotation is needed. The calculated results show that it is impossible to cover 180 degree by only controlling one quadrupole. As an optimized result, two quadruple currents are changed from -3.5A to 3.5A, to cover about 170 degrees.

In order to minimize the nonlinear effects, the beam current must be small. In this experiment, 8 mA photoemission electron beam is chosen. Since the FWHM of the current pulse is only about 5 ns, the images on the phosphor screen are very dim. In the experiment, in order to get an accurate transverse distribution of the electron beam, the laser repetition rate is 15Hz and more than 100 frames of pictures are taken by the CCD camera. All the pictures are then added up and normalized to get the transverse distribution of the electron beam at one quadrupole currents condition.

The transverse distribution of the electron beam is changed under the different quadrupole currents. The distribution profile on x or y direction is calculated, as the $C(l,\phi)$ in the inverse Radon transform in equation (4.3). With the profile data under about 60 different combinations of quadrupole currents, the phase spaces of an 8 mA 5 ns photoemission electron beam at 191 cm from electron gun are reconstructed and shown in Figure 4.2. The unnormalized 4*RMS (effective) emittance of this beam in x-x' phase space is 8.5 mm-mrad and in y-y' phase space is 16.2 mm-mrad. The difference between ε_x and ε_y is mainly due to the bad quality of x-x' phase space. The effective emittance of the photoemission beam in y direction is almost same as that of 7 mA thermionic electron beam, which is 15.5 mm-mrad [27].
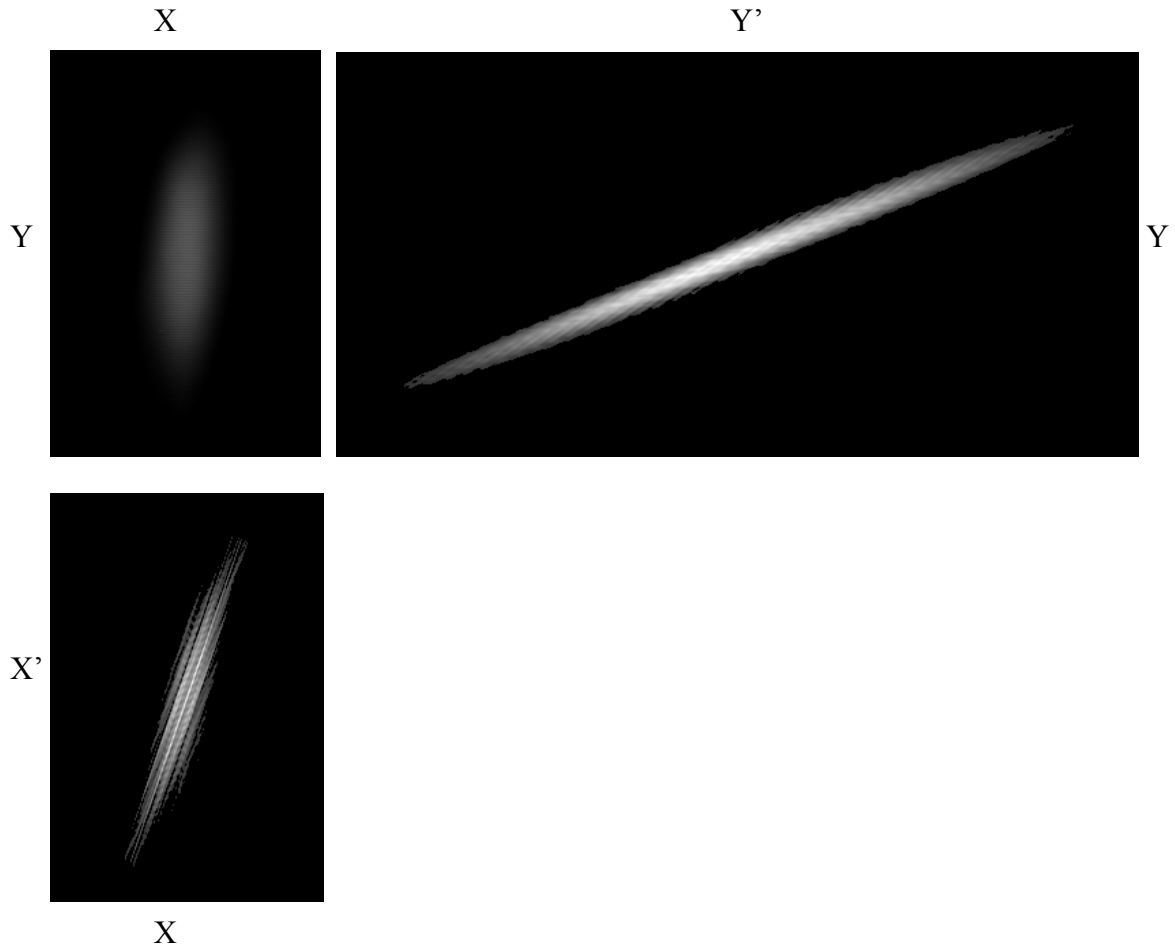
Figure 4.2 The phase space of photoemission electron beam. The y vs. x figure is the beam cross-section distribution. The x' vs. x figure is the phase space in x direction. The y' vs. y figure is the phase space in y direction.

4.3 Summary and discussions

The transverse phase space of an 8 mA photo-emission electron beam is studied experimentally. Both x vs. x' and y vs. y' phase space are reconstructed, and the emittance is calculated.

However, this is only a preliminary tomography investigation of the photoemission electron beam. Several improvements need to be incorporated in the future.

The main problem of this photoemission electron beam tomography is that the beam current is changes with time. The image at the phosphor screen is the result of time integration for the whole beam. For a regular rectangular thermionic emission beam, the current is constant except a very short head and tail. However, for photoemission beam the beam current is varying all the time. Thus, the beam radius and transverse distribution always fluctuate. The final phase space figure is a result of time integration. In order to get the phase space figures for each slice of the photoemission electron beam, the slit-collector can be used to get the time dependent beam distribution profile. With this data, the phase space of each time slice of the beam can be reconstructed.

Because the space-charge force also plays an important role in the 8 mA photoemission electron beam, it should be included in the propagation matrix. Since the beam current is time dependent, the envelope of this beam should be calculated for different slices. Then the space-charge force can be derived from the beam envelope and used in the propagation matrix.

Chapter 5: Conclusion

The main purpose of this thesis is to study the dynamics of longitudinal space-charge waves on electron beams, which are produced by initial pure-density modulation.

An analytical theory of the longitudinal space-charge wave in a uniform focusing channel is discussed first. The single particle motion equation with initial conditions shows that the small sinusoid initial modulation in the main electron beam is the superposition of two eigenfunctions, the fast space-charge wave and the slow space-charge wave. The sound speed (the velocity of the space-charge wave in the beam frame) is derived by the cold-fluid model. The evolution of an arbitrary localized perturbation is expressed analytically by using double Laplace transforms on the continuity equation and the momentum transfer equation in the cold-fluid model. The results for the initial pure-density modulation condition are derived. The theoretical analysis shows that the single peak pure-density perturbation splits into two perturbations and moves away from each other. The small sinusoid modulation on the main beam is also calculated. The initial pure-density modulation completely transfers to the pure-energy modulation and then reverts back. Correspondingly, the period length of the oscillation between the density and energy modulation is calculated.

A WARP 2-D (RZ) simulation program is set up to simulate the pure-density modulation evolutions. While the beam transport experiments (100 ns, 20 mA, 10 keV) are performed in a FODO focusing channel of conducting pipes, the simulations are done in a uniform focusing channel. The simulation results of single peak pure-density perturbation and small sinusoid modulation are presented. For the 2 mA single-peak

perturbation and sinusoid modulation, the simulation results agree well with the theoretical analysis. For the 20 mA single peak perturbation, some nonlinear and instability phenomena show up.

The propagation of the single peak pure-density perturbation is experimentally studied for the first time. An ultraviolet laser (355 nm) is used to generate the photoemission electrons, which have almost the same energy distribution as the thermal emission electrons. A 100 ns main beam with 5 ns photoemission perturbation at the beam bunch center propagates in the UMER for about 10 meters. The initial single peak perturbation splits into two perturbations due to the fast and slow space-charge waves. The sound speed is measured for the different combinations of main beam current and perturbation current. The sound speed of the space-charge wave increases with main beam currents, similar to the sound wave propagation at different speeds in gases, liquids and solids. The sound speed increases when the perturbation is larger at a constant main beam current due to the nonlinear effects. The experimental results are in good agreements with the theories and simulations.

In the second part of the thesis, the experimental result of the transverse phase space of an 8 mA photoemission electron beam is determined using a computerized tomographic technique, from which the emittance is also calculated. In the future, the study of time dependent phase space is important, since the beam current changes with time in the photoemission electron beam.

Bibliography

[1]   V. K. Zworykin et al., "Electron Optics and the Electron Microscope," Wiley, New York, 1945.

[2]   M. Reiser, "Theory and Design of Charged Particle Beams," Wiley & Sons, New York, 1994.

[3]   O. Klemperer, "Electron Optics, Cambridge University Press," Cambridge, 1953.

[4]   Proceedings of the 1988 International Symposium on Heavy Ion Inertial Fusion, GSI, Darmstadt, FRG, June 28-30, 1988, Nucl. Instr. Meth., A 278, 1, 1989.

[5]   Proceedings of the 1986 Symposium on Heavy Ion Inertial Fusion, AIP, Conference Proceedings 152. New York, 1986.

[6]   E. P. Lee, Nuovo Cimento, 106A, 1993.

[7]   J. Wei, et al, "Spallation Neutron Source Ring - Status, Challenges, Issues, and Perspectives", Proc. IEEE 2003 PAC, Portland, OR, p. 571, 2003.

[8]   T. C. Marshall, "Free Electron Laser," Macmillan Pub. Co., New York, 1985.

[9]   P. G. O'Shea, Personal Communication, Aug. 2004.

[10]   J. D. Lawson, "The Physics of Charged-Particle Beams," Ch.4, Clarendon Press, Oxford, 1988.

[11]   J. Harris, Master Thesis, University of Maryland, 2002.

[12]   R. Kishek, Personal Communication, Aug. 2004.

[13]   D. X. Wang, "Experimental Studies of Longitudinal Dynamics of Space-Charge Dominated Electron Beams," Doctoral Dissertation, University of Maryland, 1993.

[14]   J. G. Wang, et al, "Longitudinal space-charge waves and instabilities in intense beams," Phys. Plasmas, 5(5), pp. 2064-2070, 1998.

[15]   H. Suk, et al, "Experiments on space-charge waves on electron beams propagating through a resistive-wall channel," J. Appl. Phys. 86, No. 3, p. 1699, 1999.

[16]   Y. Zou, "Experimental Studies on Resistive-Wall Instability and Development of Beam Diagnostics for the University of Maryland Electron Ring Facility," Doctoral Dissertation, University of Maryland, 2000.

[17]   D. A. Callahan, et al, "The longitudinal wall impedance instability in a heavy-ion fusion driver," J. Appl. Phys. 81 (8), p. 3398, 1997.

[18]   N. A. Krall, et al, "Principles of Plasma Physics," McGraw-Hill, New York, 1973.

[19]   J. G. Wang, et al, "Generation of Space-Charge Waves due to Localized perturbations in a Space-Charge Dominated Beam," Physical Review Letters Vol. 71, No. 12, 1993.

[20]   The calculation is done based on a matlab code developed by Y. Zou.

[21]   P. G. O'Shea, Personal Communication, May 2004.

[22]   Cooperation with I. Haber.

[23]   M. Walker, Presentation for the DOE review, May 2004.

[24]   P. G. O'Shea, et. al., "The University of Maryland Electron Ring (UMER)," Nuclear Instruments and Methods in Physics Research A 464, pp. 646-652, 2001.

[25]   UMER website: http://www.ireap.umd.edu/umer .

[26]   H. Li, et al, "Simulation studies on matching of space-charge-dominated beams for the University of Maryland Electron Ring," Nucl. Instr. Meth., A 519, pp. 405-411, 2004.

[27] H. Li, "Control and transport of intense electron beams," Doctoral Dissertation, University of Maryland, 2004.

[28] B. Leblond, "Short pulse photoemission from a dispenser cathode under the 2nd, 3rd and 4th harmonics of a picosecond Nd:YAG laser," Nucl. Instr. Meth., A 317, pp. 365-372, 1992.

[29] B. Quinn, et al, "Design and testing of a fast beam position monitor," Proceedings of the 2003 Particle Accelerator Conference, 2003.

[30] Minilite and PIC Nd:YAG Laser User Manual, Continuum Corporation.

[31] H. Bergeret, et al, "Short pulse photoemission from a dispenser cathode," Nucl. Instr. Meth., A 301, No.3, pp. 389-394,1991.

[32] A. C. Kak, M. Slaney, "Principles of Computerized Tomographic Imaging," the Institute of Electrical and Electronics Engineers, Inc., New York, 1988.

[33] S. Hancock, et al, "Tomographic reconstruction of transverse phase space from turn-by-turn profile data," Proceedings of 1999 Particle Accelerator Conference, New York, 1999.

[34] S. Hancock, et al, "Longitudinal phase space tomography with space charge," Physical Review Special Topics-Accelerators and Beams, Vol. 3, No. 12, Dec. 2000.

[35] J. Chen, et al, "Emittance measurement by using DUO image pattern of cherenkov radiation," Proceedings of 2003 Particle Accelerator Conference, pp. 2580-2582, 2003.